Combining seismic signal dynamic inversion and numerical modeling improves landslide process reconstruction

Yan Yan[a,c], Yifei Cui[b]*, Jiaojiao Zhou[a], Xinghui Huang[d], Wengang Zhang[e], Shuyao Yin[a], Jian Guo[b],

Sheng Hu[f]

[a] Key Laboratory of High-Speed Railway Engineering, MOE/School of Civil Engineering, Southwest

Jiaotong University, Chengdu 610031, China

[b] State Key Laboratory of Hydroscience and Engineering, Tsinghua University, Beijing 100084, China

[c] Institute of Geographic Sciences and Natural Resources Research, Chinese Academy of Sciences, Beijing

100101, China

[d] China Earthquake Networks Center, Beijing 100045, China

[e] School of Civil Engineering, Chongqing University, Chongqing 400045, China

[f] College of Urban and Environmental Sciences, Northwest University, Xi'an 710127, China

*Corresponding author: Yifei Cui, e-mail: yifeicui@mail.tsinghua.edu.cn

Abstract

Landslides present a significant hazard for humans, but continuous landslide monitoring is not yet possible due to their unpredictability. In recent years, numerical simulation and seismic inversion method have been used to provide valuable data for understanding the entire process of landslide movement. However, each method has shortcomings. Dynamic inversion based on long-period seismic signals gives the force-time history of landslide using empirical Green's function, but lack of detailed flowing characteristics of the hazards. Numerical simulation can simulate the entire movement process, but results are strongly influenced by choice of modelling parameters. Therefore, developing a method for combining those two techniques has become a focus for research in recent years. In this study, we develop such a protocol based on analysis of the 2018 Baige landslide in China. Seismic signal inversion results are used to constrain and optimize the numerical simulation. We apply the procedure to the Baige event and, combined with field/geological survey, show it provides a comprehensive and accurate method for dynamic process reconstruction. We found that the Baige landslide was triggered by detachment of the weathered layer, with severe top fault segmentation. The landslide process comprised four stages: initiation, main slip, blocking, and deposition. Multi-method mutual verification effectively reduces the inherent drawbacks of each method, and multi-method joint analysis improves the rationality and reliability of the results. The approach outlined in this study could help better understand the landslide dynamic

process.

1. Introduction

Landslides present a significant hazard for humans, the number of fatalities resulting from non- coseismic landslides between 2004 and 2016 averaged 4,000 per year (Froude and Petley, 2018). However, they cannot be continuously monitored due to their unpredictability and difficulty of detection (Chen et al., 2013; Yamada et al., 2013; Feng et al., 2016; Wang et al., 2020b), and the landslide movement process cannot be fully understood through post-event field investigation and remote sensing alone. Hence, to aid warning and prevention of landslide hazards and reduce associated losses, there is an urgent need to develop alternative methods to enable in-depth investigation of the dynamic characteristics of landslide generation and movement.

Landslide movement generates seismic signals that propagate to the surrounding area. The development of environmental seismology and construction of global seismic networks (Dammeier et al., 2016) means the seismic signals generated by landslide movement can be quantitatively recorded by nearby seismic stations (Walter et al., 2012; Yamada et al., 2012; Chen et al., 2013; Yamada et al., 2013). Seismic signals generated by landslides reflect the duration, location, and scale of the event (Kao et al., 2012; Yamada et al., 2012; Chen et al., 2013); seismic signal analysis is increasingly used for landslide hazard monitoring and early warning, but it also offers a research tool for understanding landslide dynamics. The size and location of landslides

64   can be estimated from the amplitude, frequency range, and time-frequency spectrum of the seismic

65   signal (Favreau et al., 2010; Moretti et al., 2012; Moretti et al., 2015), along with timing of the

66   event (Sakals et al., 2011; Zhang et al., 2019), and landslide dynamics (Yamada et al., 2013; Hibert

67   et al., 2015; Jiang et al., 2016). The method of detecting, locating, and identifying landslide events

68   using broadband seismograph records is based on associating seismic signals with landslide

69   characteristics. Some progress has been made in interpreting landslide seismic signals, but signal

70   recognition is often hindered by interference from seismic signals generated by other factors (Feng,

71   2011; Zhao et al., 2015; Fuchs et al., 2018). Several methods have been developed to solve signal

72   noise pollution (Helmstetter and Garambois, 2010; Feng, 2011), but analysis of landslide dynamic

73   characteristics and reconstruction of landslide processes is still subject to errors and inaccuracies.

74   Recently, filtering of seismic signals has been successfully applied to reconstruct dynamic

75   landslide processes, allowing transition stages to be identified that are difficult to derive from field

76   analysis alone (Yan et al., 2020a, 2020b).

77   Combining seismic signal analysis with dynamic inversion can improve the extraction of

78   landslide dynamic characteristics. Landslide dynamic inversion using long-period seismic records

79   based on a single-force source model (Kanamori and Given, 1982; Kanamori et al., 1984;

80   Hasegawa and Kanamori, 1987; Dahlen, 1993; Fukao, 1995) and a static point source assumption

81   has been widely adopted to study landslide kinematics (Allstadt, 2013; Ekström and Stark, 2013;

82   Yamada et al., 2013; Hibert et al., 2014, 2015; Moore et al., 2017; Gualtieri and Ekström, 2018;

83   Li et al., 2019b; Sheng et al., 2020; Zhao et al., 2020). Predictive relationships between the

84   maximum inverted forces and sliding volume can be derived from inverted landslide force histories

85 (Ekström and Stark, 2013; Chao et al., 2016). Landslide basal friction is estimated directly using

86 a block model (Brodsky et al., 2003; Allstadt, 2013; Yamada et al., 2013; Zhao et al., 2015; Yu et

87 al., 2020) or obtained from seismic analysis coupled with numerical simulation (Moretti et al.,

88 2012, 2015; Yamada et al., 2016, 2018). Although numerical simulation of landslide dynamic

89 processes has achieved remarkable results, there are issues with each of the following three main

90 approaches. The continuous medium approach, including smoothed particle hydrodynamics (SPH)

91 (Pastor et al., 2014), material point method (MPM) (Soga et al., 2016), finite element method

92 (FEM) (Muceku et al., 2016), finite volume method (FVM) (Pitman et al., 2003), and finite

93 difference method (FDM) (Shen et al., 2020), is not very effective in describing particle separation

94 and internal fracture of rockslides. The thin-layer models are based on the thin-layer approximation

95 and depth-averaging of the Navier–Stokes equations without viscosity, but a main issue is low

96 computational accuracy (Moretti et al., 2012, 2015; Yamada et al., 2016, 2018). The discrete

97 element approach utilizes software such as particle flow code (PFC) (Lo et al., 2011; Zhang et al.,

98 2020a) and DEM solutions (EDEM) (Wang et al., 2020c), but a major issue is low computational

99 efficiency. MatDEM uses an innovative matrix discrete element method and three-dimensional

100 contact algorithm, which can realize the efficient numerical simulation of millions of particles (Liu

101 et al., 2013, 2017). However, studies utilizing MatDEM mostly determine the correctness of

102 landslide simulation through comparison with post-event landslide characteristics derived from

103 field investigation (Liu et al., 2017), which may not represent dynamic processes. An alternative

104 approach that offers potential is to use seismic signal inversion as the constraint on landslide

105 dynamic process (Yamada et al., 2016, 2018).

106   In this study, we use long period seismic signal to obtain the dynamic characteristics of Baige

107   landslide, China, which occurred on October 10, 2018 (termed as the "10.10" event). Combined

108   with the inversion results, the landslide process was reconstructed by numerical simulation.

109   Through seismic signal analysis, landslide dynamic inversion and numerical simulation, combined

110   with the post-event field investigation, we try to provide an improved characterization of the

111   landslide movement process.

112

## 2. Study area and data sources

114   A massive landslide occurred at Baige, on the eastern Qinghai-Tibetan Plateau, China, on

115   October 10, 2018 (termed as the "10.10" event) (Fig. 1). The landslide caused the blockage of the

116   main stream of Jinsha River and formed a barrier lake. On October 12, the water of the barrier lake

117   began to discharge naturally until all the discharge was completed on October 13. On November

118   3, 2018, the rock and soil mass at the trailing edge of the slide source area of the first Baige

119   landslide was unstable again, causing the second landslide. It has been studied by many researchers,

120   Xu et al. (2018) and Deng et al. (2019) analysed the formation mechanism and process of the

121   landslide, and found that the site is in the Jinsha River suture zone, where the influence of multiple

122   tectonic movements provides a complicated regional tectonic profile; the main fault structures

123   trend NW, within the Jiangda-Bolo-Jinshajiang fault zone (Fig.2). Ouyang et al. (2019), Fan et al.

124   (2019a) and Wang et al. (2020c) carried out numerical simulation analysis of Baige landslide. In

125   this study, only the "10.10" Baige landslide was studied. The landslide can be divided into four

126   areas, namely, shear, main slip, blocking, and deposition, with maximum and average thicknesses

127   of 80 and 50 m (Fig. 1c). We used terrain data from Ouyang et al. (2019), comprising a 10 m

128   resolution pre-landslide Digital Elevation Model (DEM) from 2017, and a 5 m resolution post-

129   slide DEM obtained through Unmanned Aerial Vehicle (UAV) photogrammetry in 2018 from field

130   investigation. Based on DEM differencing, total landslide volume was calculated as $1.96 \times 10^7 \, \mathrm{m}^3$.

131   The altitude range of the initiation zone is 3523 to 3730 m. Most of the rock mass that collapsed

132   from the steep back wall accumulated at an elevation of 3100 to 3300 m, in an area of gentle slope

133   angle from 20 to 25°.

134
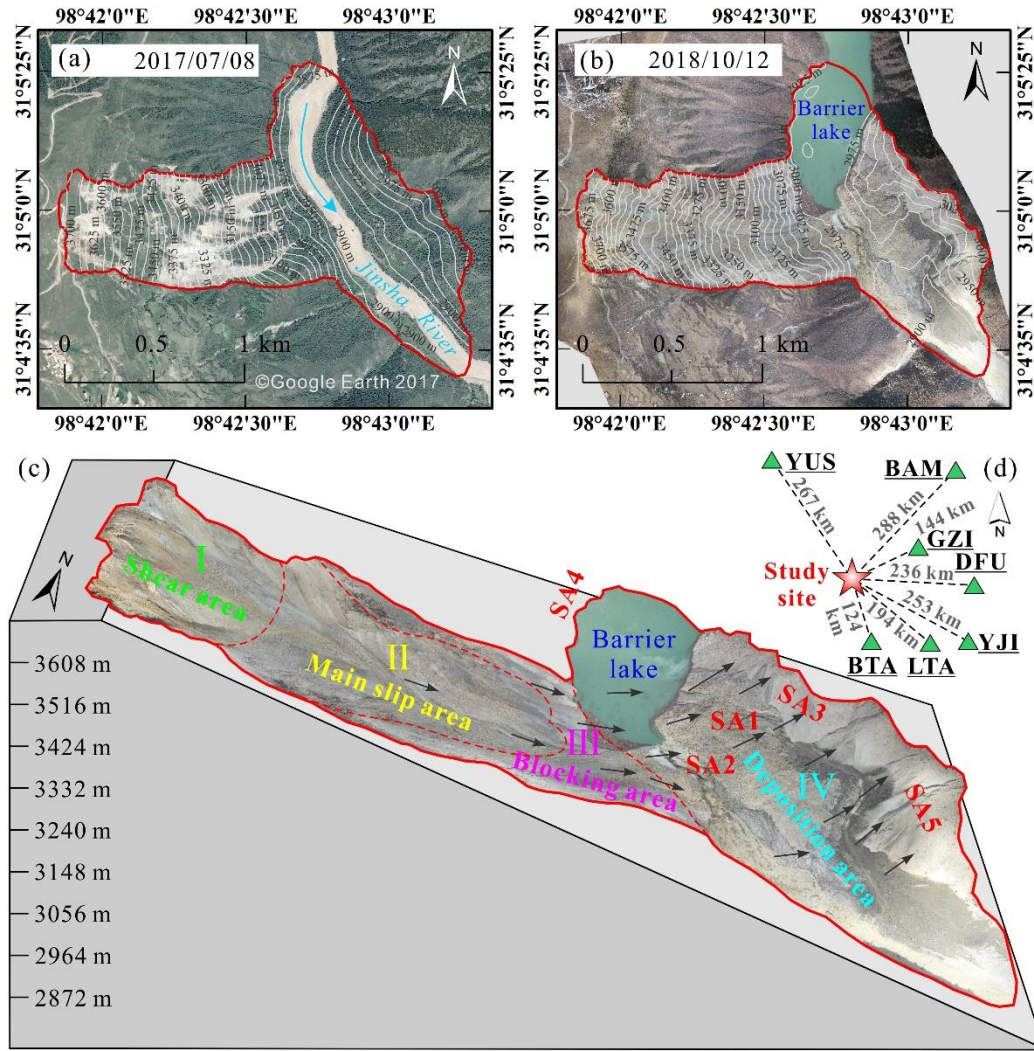
Fig. 1. Location of the study area. **(a)** Digital Orthophoto Map (DOM) of Baige landslide 2017; **(b)** DOM of Baige landslide after the 2018 event; **(c)** Schematic cross-section with remote sensing overlay showing key features of the Baige landslide (SA1 and SA2 is two main accumulation zone, the debris of SA1 is main from shear area, while SA2 main from main slip area and blocking area; SA3 is the left bank of the river, scoured by landslide debris; SA4 is a small area of the right bank scoured by landslide debris; SA5 is the downstream left bank, which is affected by the landslide body mix with the sandblasting water); **(d)** Location of the Baige landslide (red star) relative to seismic stations (green triangles) used in the study. The remote sensing image map data of Fig 1.a. is from the © Google Earth 2017, and the data of Fig 1.b. and Fig 1.c. are from the authors' own Unmanned Aerial Vehicle (UAV) photography measurements.

147
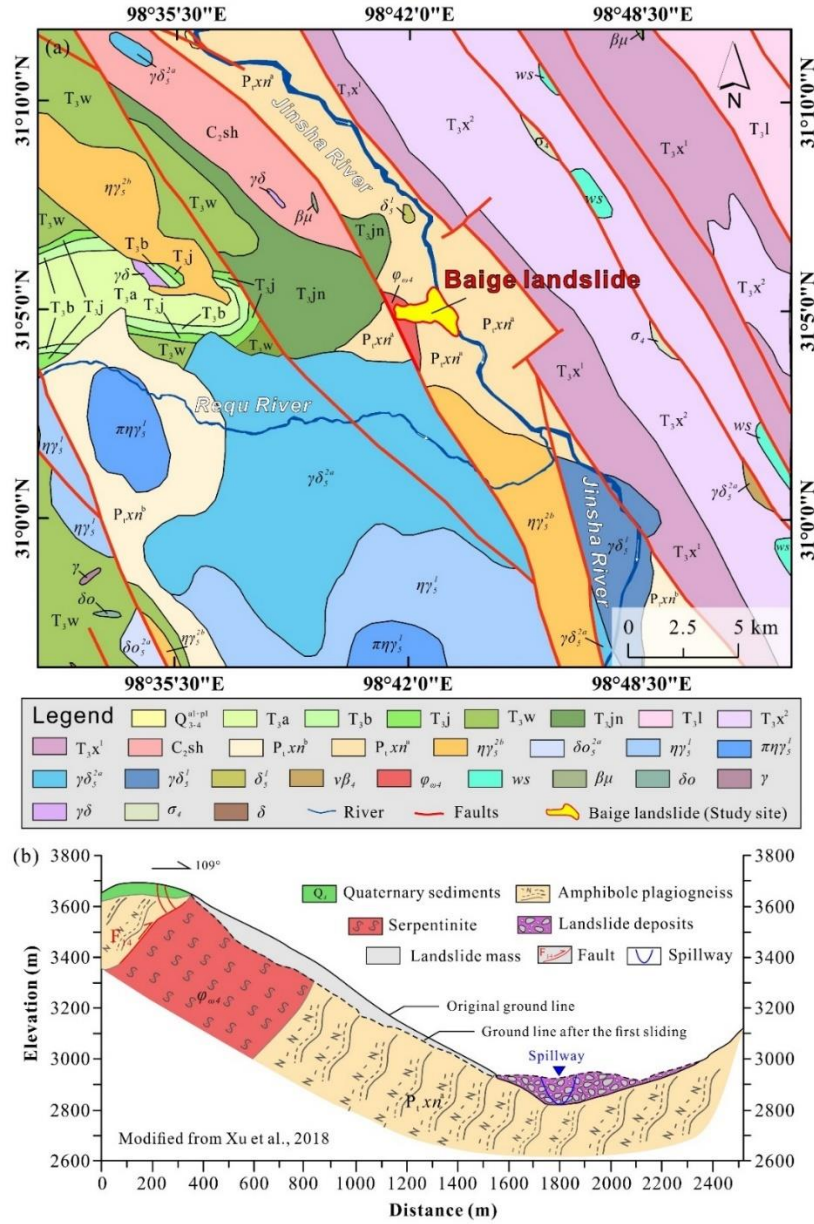
Fig. 2. Geology of the study area. **(a)** Geological map of the Baige landslide area (Q_{3-4}^{al-pl}:

Quaternary Holocene Upper Pleistocene; T_3a, T_3b, T_3j, T_3w, T_3jn, T_3l, T_3x^2, T_3x^1: Upper

Triassic; C_2sh: Upper Carboniferous; P_txn^b, P_txn^a: Proterozoic; $n\gamma_5^{2b}$, δo_5^{2a}: Yanshan period;

$n\gamma_5^1$, $\pi n\gamma_5^1$, $\gamma\delta_5^{2a}$, $\gamma\delta_5^1$, δ_5^1: Indosinian; $v\beta_4$, $\varphi\omega_4$, σ_4: Variscan; ws: Detached block; $\beta\mu$:

Diabase-porphyrite; δo: Quartz diorite veins; γ: Granite veins; $\gamma\delta$: Granodiorite dikes; δ: Diorite

veins.); **(b)** Cross-section of the landslide showing the geological profile. The geological map data

in Figure 2a is from Li et al., 2019a, and the cross-section in Figure 2b is modified from Xu et al.,

2018.

9

156

We selected broadband seismic signals from seven seismic stations that are distributed around

the landslide with adequate azimuth coverage (Fig. 1d) to carry out the analysis. Landslide force

history inversion uses long-period seismic waveforms and thus requires that the ambient noise at

periods of tens of seconds should be at a low level in the study area. We used the probabilistic

power spectral density (PSD) technique (McNamara and Buland, 2004) to characterize the

background seismic noise. As illustrated by the PSD of the vertical component for seismic station

BTA (Fig. 3), the main seismic energy is distributed between the new high noise model (NHNM)

and the new low noise model (NLNM) (Peterson, 1993), indicating that the study area has a

relatively good seismic observation environment. Before carrying out the dynamic inversion, we

will calculate the SNR for each seismic trace and use it to determine if the trace will be used in the

inversion, about which a detailed description can be found in section 4.2 Dynamic inversion of

landslide.

169

170
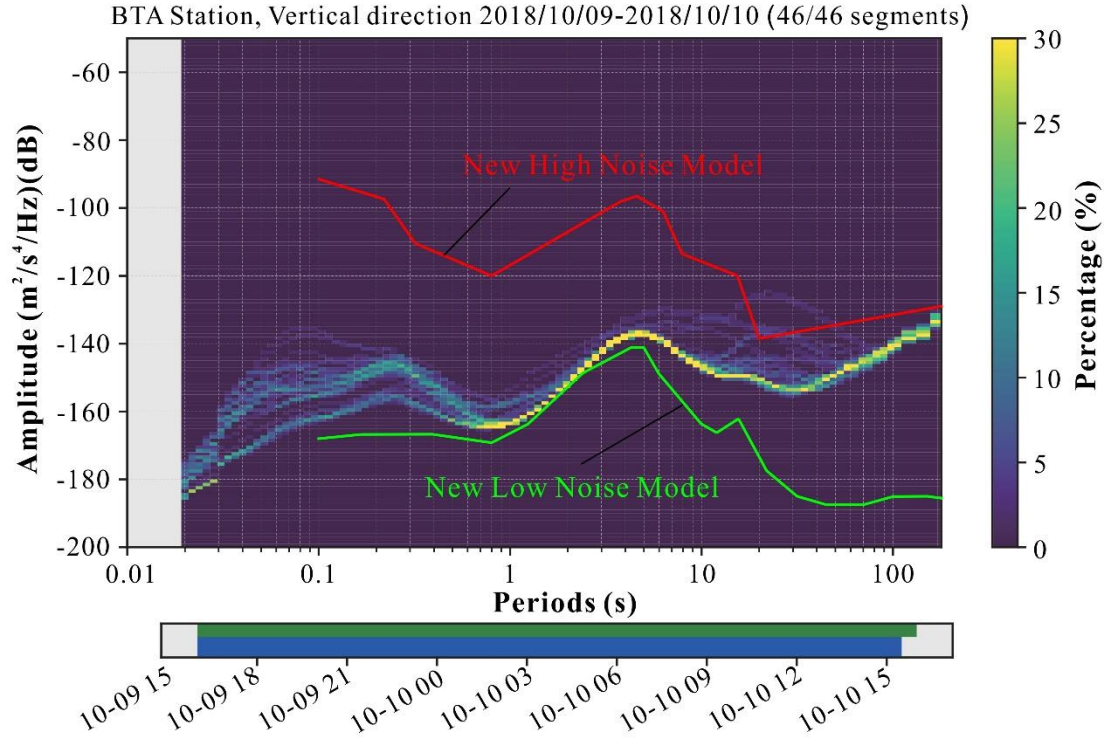
Fig. 3. Probabilistic power spectral density of the vertical component at seismic station BTA. Red line in the PSD image is NHNM and green line is NLNM. Below the PSD image is a visualization of the data basis for the calculation. The top row shows data fed into the calculation with green patches representing available data. The bottom row in blue shows the single PSD measurements that go into the histogram.

3. Methodology

3.1 Seismic data analysis

We used short-time Fourier transform (STFT) and PSD to quantitatively analyze the seismic signals for Baige landslide (Yan et al., 2020a, 2020b). A time-frequency domain transform of the seismic signal using STFT allowed information on both the time and frequency domain distributions of the seismic signal to be obtained. The power of each unit of frequency for each frequency band component that corresponds to a specific moment was estimated based on the PSD of the seismic signal in the frequency domain.

11

3.2 Landslide force history inversion

Assuming the landslide source is represented as a series of time-varying forces acting on a static point, synthetic seismograms $u_n(\boldsymbol{x}, t)$ at the seismic station located at $\boldsymbol{x}$ can be computed by convolution of force $f_i(\boldsymbol{x_0}, t_0)$ at $\boldsymbol{x_0}$ with nine-component Green's functions $G_{ni}(\boldsymbol{x}, t; \boldsymbol{x_0}, t_0)$ (Moretti et al., 2012; Allstadt, 2013; Ekström and Stark, 2013; Yamada et al., 2013; Hibert et al., 2014; Li et al., 2017; Gualtieri and Ekström, 2018),

$$u_n(\boldsymbol{x}, t) = G_{ni}(\boldsymbol{x}, t; \boldsymbol{x_0}, t_0) * f_i(\boldsymbol{x_0}, t_0) \tag{1}$$

where $*$ denotes convolution and bold type face indicates a vector. The Einstein summation convention is assumed in the equation. The convolution can be rewritten as matrix product,

$$\boldsymbol{u}_n = [\boldsymbol{G}_{n1} \quad \boldsymbol{G}_{n2} \quad \boldsymbol{G}_{n3}] \begin{bmatrix} \boldsymbol{f}_1 \\ \boldsymbol{f}_2 \\ \boldsymbol{f}_3 \end{bmatrix} \tag{2}$$

Suppose there are N seismic traces,

$$\begin{bmatrix} \boldsymbol{u}_1 \\ \vdots \\ \boldsymbol{u}_N \end{bmatrix} = \begin{bmatrix} \boldsymbol{G}_{11} & \boldsymbol{G}_{12} & \boldsymbol{G}_{13} \\ \vdots & \vdots & \vdots \\ \boldsymbol{G}_{N1} & \boldsymbol{G}_{N2} & \boldsymbol{G}_{N3} \end{bmatrix} \begin{bmatrix} \boldsymbol{f}_1 \\ \boldsymbol{f}_2 \\ \boldsymbol{f}_3 \end{bmatrix} \tag{3}$$

Use $\boldsymbol{u} = \begin{bmatrix} \boldsymbol{u}_1 \\ \vdots \\ \boldsymbol{u}_N \end{bmatrix}$, $\boldsymbol{G} = \begin{bmatrix} \boldsymbol{G}_{11} & \boldsymbol{G}_{12} & \boldsymbol{G}_{13} \\ \vdots & \vdots & \vdots \\ \boldsymbol{G}_{N1} & \boldsymbol{G}_{N2} & \boldsymbol{G}_{N3} \end{bmatrix}$, and $\boldsymbol{f} = \begin{bmatrix} \boldsymbol{f}_1 \\ \boldsymbol{f}_2 \\ \boldsymbol{f}_3 \end{bmatrix}$, we get the linear forward model

$$\boldsymbol{u} = \boldsymbol{G}\boldsymbol{f} \tag{4}$$

We use $\boldsymbol{u}_o$ to denote observed seismic records and define the 2-norm of the vector difference between $\boldsymbol{u}_o$ and $\boldsymbol{u}$ as an objective function,

$$\boldsymbol{o} = \|\boldsymbol{u} - \boldsymbol{u}_o\|_2 \tag{5}$$

An optimal solution of the forces can be obtained in a least-square sense,

$$\boldsymbol{f} = (\boldsymbol{G}^T\boldsymbol{G})^{-1}\boldsymbol{G}^T\boldsymbol{u}_o \tag{6}$$

The landslide force history can be reconstructed by direct deconvolution of the observed seismograms with Green's functions, which can be readily performed in both time and frequency

207 domains (Allstadt, 2013; Yamada et al., 2013; Li et al., 2017). We calculated Green's Function at

208 the landslide location for each seismic station, using a matrix propagation method (Wang, 1999)

209 and a 1-D layered velocity model from Crust1.0 (https://igppweb.ucsd.edu/~gabi/crust1.html).

210 Once the landslide force history f was inverted, based on Newton's third law of motion, the

211 forces acting on the sliding mass could be obtained by multiplying the inverted force history by -

212 1 (Kanamori and Given, 1982; Yamada et al., 2013; Gualtieri and Ekström, 2018). And then the

213 forces acting on the sliding mass can be used to calculate its velocity and displacement

214 distributions for a given mass (Li et al., 2019c; Yu et al., 2020), or to estimate the sliding mass by

215 minimizing discrepancies with independently derived sliding trajectories (Hibert et al., 2014),

216 using the following equations,

217 $$\boldsymbol{v} = -\int \frac{\boldsymbol{f}}{m} dt \qquad (7)$$

218 $$\boldsymbol{s} = -\iint \frac{\boldsymbol{f}}{m} dt \qquad (8)$$

219

220 3.3 Numerical modeling

221 3.3.1 Discrete element method

222 To quantitatively analyze the process of landslide initiation, movement, and accumulation for

223 the "10.10" Baige event, we used MatDEM software, which is based on the matrix discrete element

224 method, to numerically simulate the landslide (Liu et al., 2017). In the discrete element method,

225 particle movement obeys Newton's second law, and particle velocity and displacement are

226 sequentially updated to simulate the dynamic process of the landslide. In MatDEM, the landslide

227 body is formed by the accumulation and cementation of particles endowed with specific

228   mechanical properties, and the contact and interaction of these particles are defined by the linear

229   elastic bonded model, as shown in Figure 4a. The normal force F_n and tangential force F_s

230   between particles can be expressed by the following formula:

$$F_n = K_n X_n \tag{9}$$

$$F_s = K_s X_s \tag{10}$$

231   where, K_n is the normal stiffness; X_n is the normal relative displacement between two

232   particles at the contact point; K_s is the tangential stiffness; and X_s is the tangential displacement.

233   In the normal direction, when the displacement between particles X_n exceeds the fracture

234   displacement X_b the connection between particles is broken and the tension is set as zero. In the

235   tangential direction, spring failure follows the Mohr-Coulomb criterion, and the tangential bond is

236   broken when tangential force exceeds maximum shear force F_{smax}, so that only sliding friction

237    $(-\mu_p F_n)$ exists between particles. The maximum normal force F_{nmax} and maximum tangential

238   force that the cementation between particles F_{smax} can withstand is:

$$F_{nmax} = K_n X_b \tag{11}$$

$$F_{smax} = F_{s0} - \mu_p F_n \tag{12}$$

239   where, F_{s0} is the shear resistance between particles and μ_p is the friction coefficient

240   between particles.
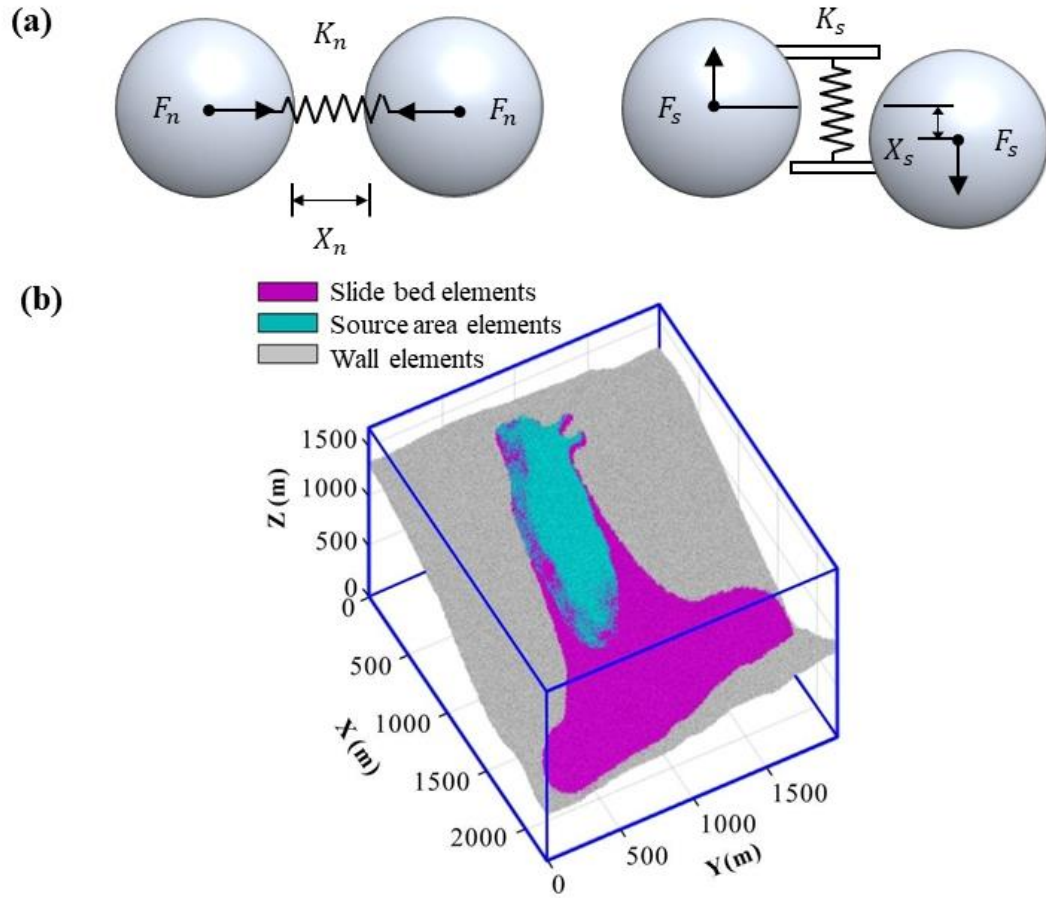
Fig. 4. Schematics showing properties of landslide particles and discrete element model. **(a)** Linear elastic bonded model; **(b)** Discrete element model of the Baige landslide (Fan et al., 2019a).

3.3.2 Discrete element model of Baige landslide

In MatDEM, the base of the landslide model is constructed of densely packed particles (20 m thick) arranged according to the topography of the slope base. The coordinates of these particles are fixed in the simulation (gray particles in Fig. 4b). The landslide area is constructed by particles accumulated in the cube model box using cutting topography of the pre- and post- landslide. Before starting the simulation, gravity is applied to particles in the sliding source area (blue particles in

15

Fig. 4b) and sedimentary layer (20–80 m thick) (purple particles in Fig. 4b); breaking the

connection between particles in the source area allows them to slide down under the action of

gravity to simulate landslide initiation. We used a simulation block of 2270×1980×1680 m, with

582,000 particles comprising 169,000 active cells for simulating landslide movement and 413,000

boundary elements to fill the geometry (bottom) and limit the range of activity (side). Average cell

size was 5 m and the real-world time 80 s.

As shown in the flow chart of Fig. 5, we used the dynamic inverted from seismic signals and

deposition characteristics as references for the DEM simulation. Initial macro parameter values,

such as Young modulus, Poisson's ratio, were based on results of laboratory tests on Baige

landslide materials from Zhou et al. (2019), the micro parameters, such as normal stiffness, shear

stiffness, breaking displacement, initial shear resistance, of DEM input can be obtained by using

the macro and micro conversion equations proposed by Liu et al. (2013) (see Appendix 1 for

details). As elastic modulus and mechanical properties in laboratory tests are usually higher than

those in large-scale rock masses in the field (Darlington et al., 2011; Hencher et al., 2014; Hoek,

2000), Liu et al. (2019) used MatDEM to simulate Xinmo landslide, set Young's modulus and

strength to about 40% of the test value, and obtained appropriate simulation results. Therefore, we

used 40% of the test value in our simulation.

The second step is to use the geometry of the deposits as a reference to adjust and obtain

reasonable simulation result. For the discrete element method, the geometry of the deposits is

affected by the bond strength between particles and the friction coefficient (An et al., 2020), which

correspond to the fracture displacement, initial shear force, and friction coefficient between

272   particles in MatDEM. Other parameters, such as normal stiffness and tangential stiffness, remain

273   constant during the simulation. Accuracy of the final landslide accumulation was evaluated by the

274   critical success index (CSI) proposed by Mergili et al. (2017), calculated as:

$$CSI = \frac{TP}{TP + FP + FN} \tag{13}$$

275   where, TP (true positive) is intersection area from both simulation and filed observation, FN

276   (false negative) is the deposition area observed from field that simulation cannot covered, and FP

277   (false positive) is the additional deposition area from simulation where no deposition is observed

278   from site. CSI ranges between 0 and 1, and the higher the value, the more accurate the simulation;

279   when CSI is 1, the simulated accumulation range coincides with the observed. An et al. (2021)

280   conducted 25 simulations by changing the parameters such as static friction coefficient, thermal

281   weakening friction coefficient and normal bond strength. The results showed that only 8 cases had

282   CSI > 0.6 and the highest CSI was 0.83. In addition, among the 15 groups of results simulated by

283   Mergili et al. (2017), the maximum CSI is 0.59. Therefore, in this study, the criterion is chosen as

284   CSI > 0.6, it can be considered that the simulated accumulation characteristics are basically

285   consistent with the actual situation.

286   The third step is to use the landslide motion velocity and displacement characteristics inverted

287   by the seismic signal as a reference to back-calibrate parameters that affect the kinematic

288   characteristics of the landslide, such as friction and average damping coefficients. The final values

289   of the parameters are shown in Table 1.

290   The accuracy of simulated and inversed landslide velocity and displacement was

291   preliminarily evaluated by the relative errors of several key points δ. Then, the square residue S^2

292   between the simulated value and the inversion value per second was calculated, and the difference

293   between the two groups of data in the landslide process was analyzed in detail. Related error δ

294   and square residue S^2 were calculated as:

$$\delta_x = \frac{X_s - X_i}{X_i} \tag{14}$$

$$S^2 = (X_s - X_i)^2 \tag{15}$$

295   where, X_s is the simulated value and X_i the inversed value. X can be replaced by landslide

296   duration T, peak velocity V_{max}, time when peak velocity achieved T_{Vmax}, and peak displacement

297   D_{max}.

298
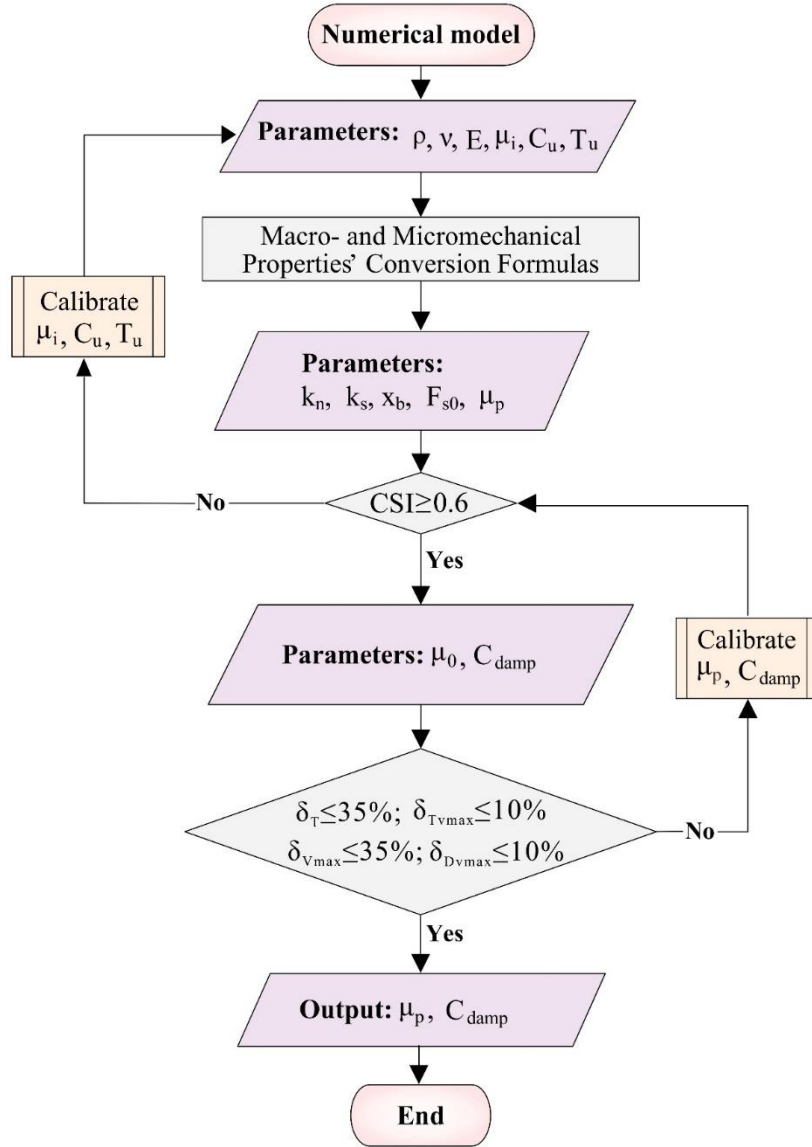
Fig. 5. Flowchart of the method of discrete element parameter adjustment based on seismic signal inversion.

Table 1. Macro- and micromechanical parameters of Baige landslide material used in the discrete element model.

Parameter	Value	Reference
Young modulus E	20 GPa	Laboratory test (Zhou et al. 2019)
Poisson's ratio v	0.2	Laboratory test (Zhou et al. 2019)
Uniaxial compressive strength C_u	30 MPa	Laboratory test & Calibrated
Uniaxial tensile strength T_u	3 MPa	Laboratory test & Calibrated
Internal friction coefficient μ_i	0.46	Laboratory test & Calibrated

Density ρ	2400 kg/m^3	Zhang et al. (2019)
Normal stiffness k_n	486 GN/m	Calculated (Liu et al., 2013)
Shear stiffness k_s	270 GN/m	Calculated (Liu et al., 2013)
Breaking displacement x_b	1.3 mm	Calculated (Liu et al., 2013)
Initial shear resistance F_{s0}	3.28 GN	Calculated (Liu et al., 2013)
Intergranular friction coefficient μ_p	0.0897	Calculated & Calibrated
Average damping coefficient C_{damp}	1.06×10^5	Calibrated

305

306

4. Results and analysis

4.1 Seismic signal analysis

The time-domain velocity curve of the seismic signal generated by the "10.10" Baige landslide is shown in Figure 6. The SNR of the vertical (V) and east (E) components is relative higher, compared with north (N) component, roughly reflecting the main slide direction of landslide is E and N. Post-event geological survey showed sliding was mainly in south-east-to-south, approximately eastwards. The driving force of the landslide is gravity, and the surface on which the mass slides is inclined at about 35°, so velocity changes in the longitudinal direction are relatively large, and the SNR of the V component of the landslide signal appears high. The morphology of the landslide path means that the landslide stage has a large east-west component and a small north-south component, and in the deposition stage, it reverses. This feature is consistent with the high SNR of the N component at the end of the landslide signal and low SNR of the E component.

320
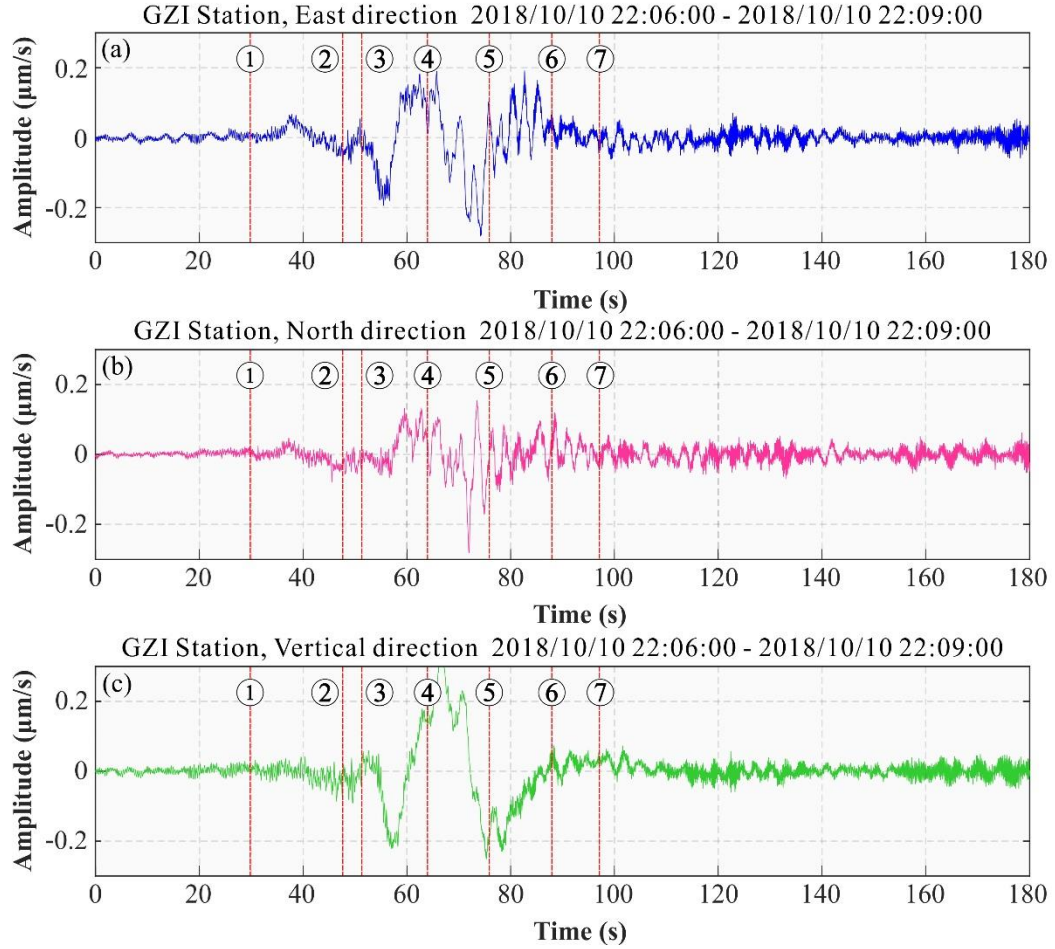
Fig. 6. Time-domain velocity signal (E\N\V direction) of the seismic generated by the Baige landslide at GZI seismic station, showing a relative high signal-to-noise ratio visually but different respectively (①~⑦ refer to the characteristic stage of the Baige landslide).

The sliding distance of the landslide was c. 600 m longitudinally and c. 100 m laterally, while the receiving stations are over 100 km away; as the sliding scale is relatively small relative to the propagation distance, we treated it as a point source. The velocity curve recorded at a seismic station is the velocity of the crustal vibration below the landslide area propagating to the station, and this is roughly determined by velocity and mass of the landslide body. Therefore, characteristics of the landslide downward movement can be obtained by analyzing the velocity curve recorded at seismic stations. The seismic signal from station GZI (Fig. 6) provides an

333   example to show the general seismic characteristics of the "10.10" Baige landslide. The time-

334   domain velocity curve recorded at GZI determines the start time of the landslide as 22:06 on

335   October 10, 2018 (all times are UTC+8), with a duration of about 76 s between 22:06:39 to

336   22:07:51. Five points of velocity change are apparent during the landslide process (Fig. 6, Table

337   2), dividing the event into three phases of acceleration and three of deceleration.

338   Due to seismic wave propagation, the start time determined by the original seismic signal at

339   the station is slightly later than the true time; what's more, the signal is mixed by longitudinal wave

340   that stack with transverse wave, which makes the ending time picked by seismic signal much latter

341   than the actual time. All these make the duration of the landslide derived from the original seismic

342   signal would be lagged and longer, compared to the real time. A more accurate landslide duration

343   can be determined by landslide force history inversion as it eliminates the propagation effect. The

344   analysis of the velocity curve recorded at seismic stations helps understand the overall

345   characteristics of the landslide and help verify the rationality of the subsequent Green's function

346   stress inversion results.

347   **Table 2.** The beginning characteristic stage of the Baige landslide river blocking event picked
348   by seismic signal recorded at GZI station.

Landslide stage						
Start Time	deceleration	acceleration	deceleration	acceleration	deceleration	End Time
22:06:39	22:06:51	22:06:54	22:07:01	22:07:12	22:07:27	22:07:51

349

350   The start and end time of sliding is demarcated on the time spectrum of the seismic curve

351   (Fig. 7); strong energy clusters appear around 22:06:39, the intensity begins to decrease at 22:06:54

352   (UTC+8), and the frequency band narrows and the energy disappears at 22:07:27 (UTC+8). The

353   time spectrum shows the landslide was concentrated between 22:06:40–22:07:01. The frequency

354   is concentrated in the 0–1 Hz range, and the low-frequency component has a high SNR (0–0.2 Hz),

355   which is conducive to dynamic inversion.

356

357
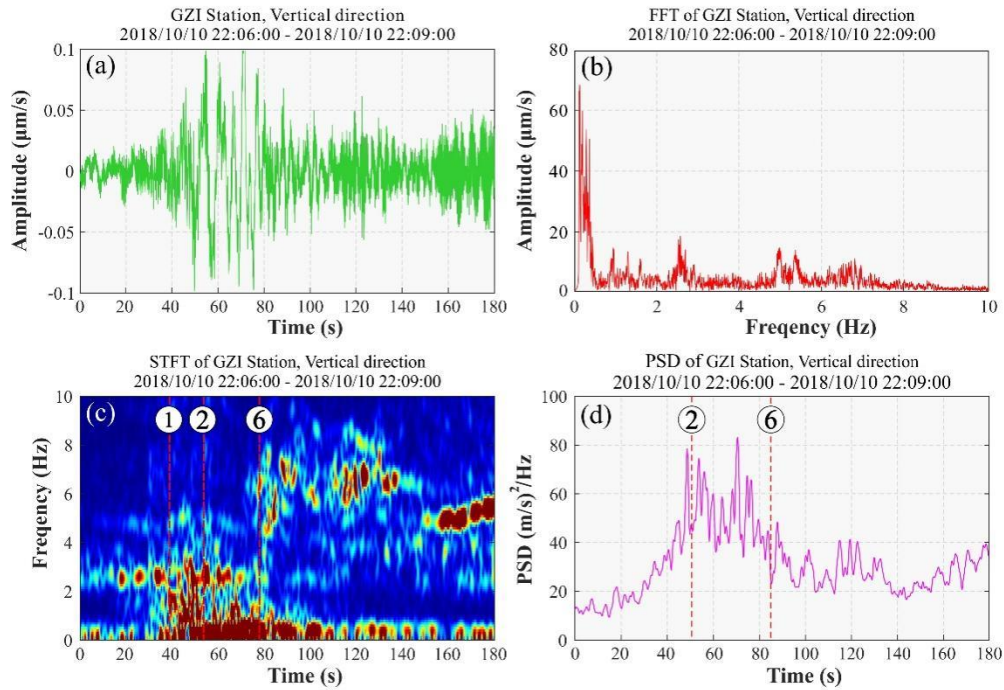
Fig. 7. Seismic signals of the Baige landslide as recorded at seismic station GZI. **(a)** Vertical seismic signal; **(b)** Frequency spectrum; **(c)** Time-frequency spectrum and the key times picked frequency from it, that is, start time, 1st acceleration and 3rd deceleration, from left to right respectively; and **(d)** Power spectral density (PSD) curve and the key times picked from it, that is 1st acceleration and 3rd deceleration.

363

364   In Figure 7d, the PSD curve is divided into three stages in the longitudinal direction, with the

365   first and third stages corresponding to slow sliding and the second stage to fast sliding. Comparing

366   with the time domain stages (as in Table 2), the first PSD stage corresponds to the first acceleration

367   and deceleration, the second stage corresponds to the second deceleration, acceleration and third

368   deceleration, and the third stage corresponds to the third deceleration. The PSD curve shows a

369 marked increase in the second stage, indicating rapid downslope sliding, with multiple large

370 fluctuations indicating rapid changes in landslide movement that are characteristic of the sliding

371 stage.

372 According to Yan et al (2021), the frequency of landslide hazard seismic signals is usually

373 low (0~5 Hz), and the morphology in the time-frequency domain and time domain presents single-

374 peak or double-peak characteristics; while the frequency of flood or high-density flow seismic

375 signals is usually high (5~50 Hz), and its morphology in the time-frequency domain and time

376 domain is mostly flat. Combined with this landslide seismic signal has relatively low frequency

377 (0~1 Hz) and the single-peak feature in time and time-frequency characteristics, apparently

378 different from the spectrum (main frequency :15~30 Hz) of the outburst flood signal on October

379 12, 2018 (Xu et al., 2018). So, we think there was no flood discharge during the landslide process.

380 ## 4.2 Dynamic inversion of landslide

381 Seismic data were processed using the following procedure before carrying out the landslide

382 force history inversion. Firstly, they were deconvolved with the instrument response to obtain

383 displacement; then a 4th-order Butterworth bandpass filter in the frequency band of 0.006–0.2 Hz

384 was then applied; and finally, the records were resampled at a sampling rate of 5 Hz. The processed

385 seismic records have a high signal-to-noise ratio (SNR) as shown in Table 3. Sixteen seismic traces

386 with an SNR larger than 10 dB were selected to carry out the inversion.

387 **Table 3.** SNR of seismic signals used in the inversion and CC and VR of the inversion results

Seismic Station		SNR	CC	VR
BTA	Z	19.19	0.96	0.90
	E	4.28	0.56	0.28
	N	8.45	0.60	0.34

GZI	Z	29.63	0.99	0.99
	E	20.39	0.99	0.98
	N	15.29	0.97	0.94
LTA	Z	24.67	0.99	0.98
	E	7.92	0.86	0.71
	N	15.12	0.97	0.94
DFU	Z	23.60	0.99	0.99
	E	17.58	0.99	0.98
	N	5.92	0.54	0.28
YJI	Z	22.58	0.98	0.97
	E	11.64	0.93	0.85
	N	16.75	0.95	0.90
YUS	Z	18.05	0.94	0.89
	E	19.39	0.98	0.97
	N	18.01	0.98	0.96
BAM	Z	21.48	0.99	0.98
	E	5.86	0.74	0.53
	N	10.91	0.94	0.88

388   The inverted force histories are shown in Fig. 8. The good fit of the synthetic and recorded

389   seismic waveforms in Fig. 9 and the high cross-correlation (CC) and variance reduction (VR)

390   between synthetic and recorded seismograms provided in Table 3 indicate the high quality of the

391   inversion results. The inverted forces show landslide initiation at 14:05:37.6, with ~61 s duration

392   of the main motion.
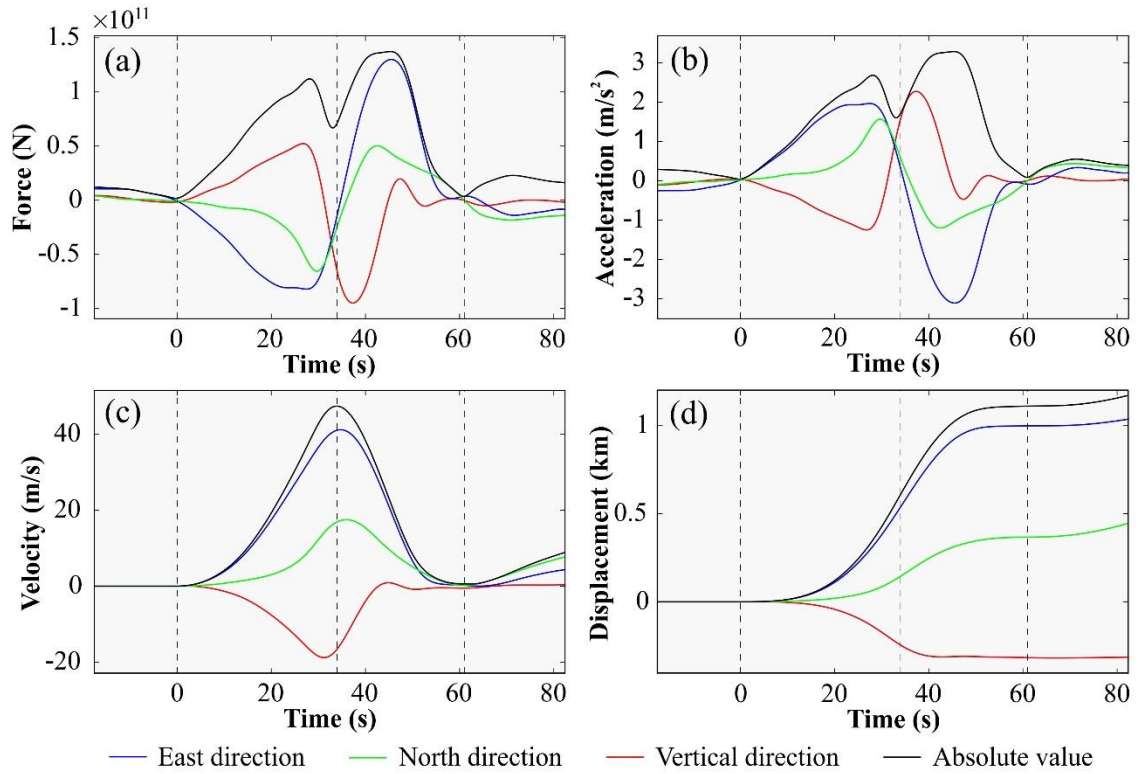
Fig. 8. Dynamic inversion used to obtain Baige landslide characteristics. **(a)** Inverted force time history; **(b)** Estimated acceleration distribution over time; **(c)** Reconstructed velocity distribution over time from the inverted landslide force time history; **(d)** Reconstructed displacement distribution over time from the inverted landslide force time history. Corresponding absolute values are shown as black lines. Dashed vertical black lines marked the landslide start and end times (the first and third ones) and the time that the sliding mass reached the maximum speed (the middle one).
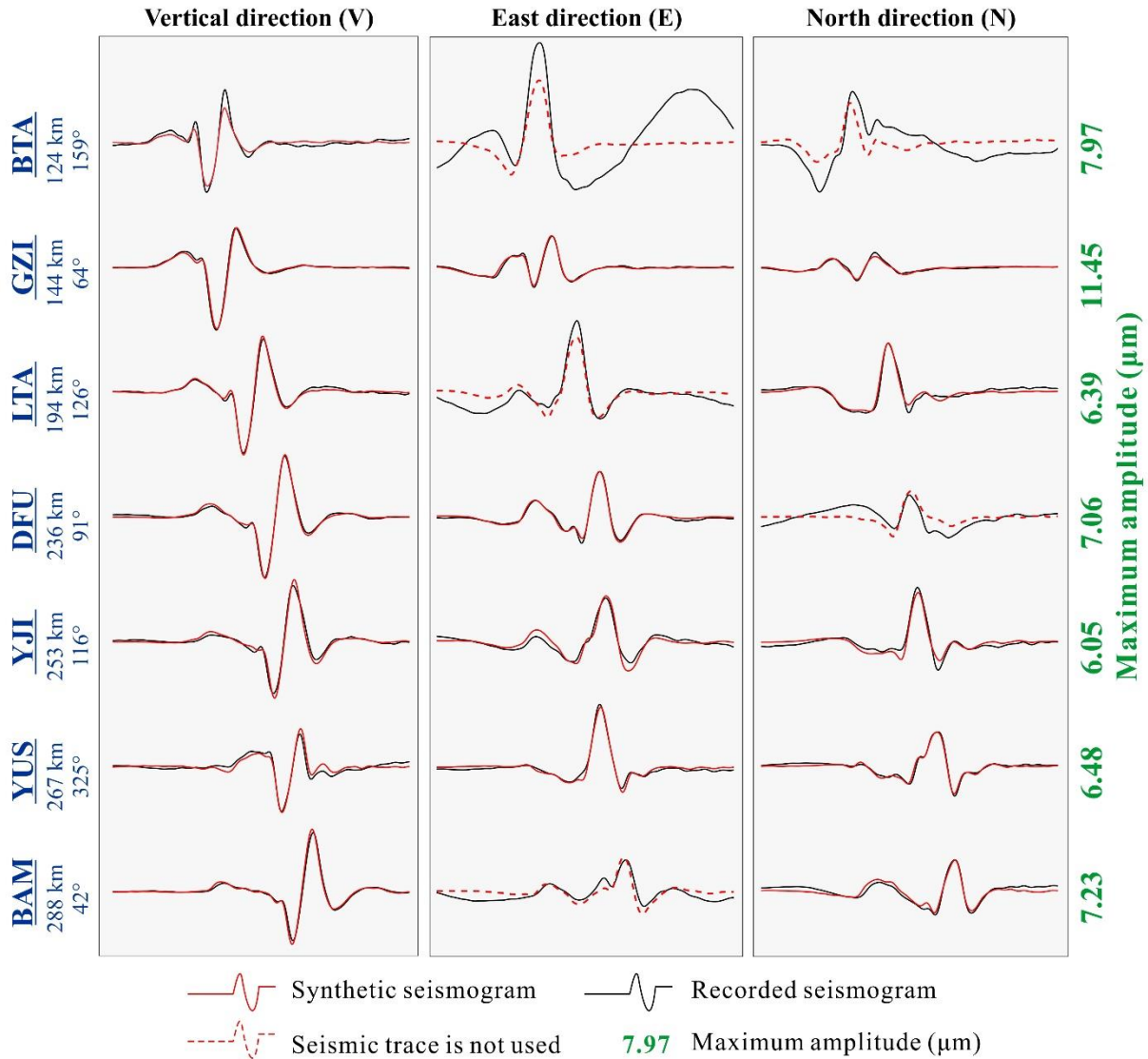
Fig. 9. Seismograms of the Baige landslide. Synthetic (red lines) and recorded (black lines) seismograms are compared. Red dotted lines indicate that the seismic trace was not used in the inversion because their SNR is smaller than 10 dB. Station name, distance from study site (km) and azimuth (degree) are given to the left of each trace (see Fig. 1d for locations), and the maximum amplitude of the three components is given in μm to the right.

By comparing the DEMs before and after the event, we determined the mass centers of the source area and the depositional area and subsequently derived the displacement of the center of the sliding mass; then, by minimizing the predicted and actual displacements, we estimated the

27

411   sliding mass as 4.2×10^{10} kg. The recovered sliding trajectory fit well with the observations, shown

412   in Fig. 10. We used the estimated sliding mass to determine the acceleration and velocity

413   distributions over time (Figs. 8b to 8d).
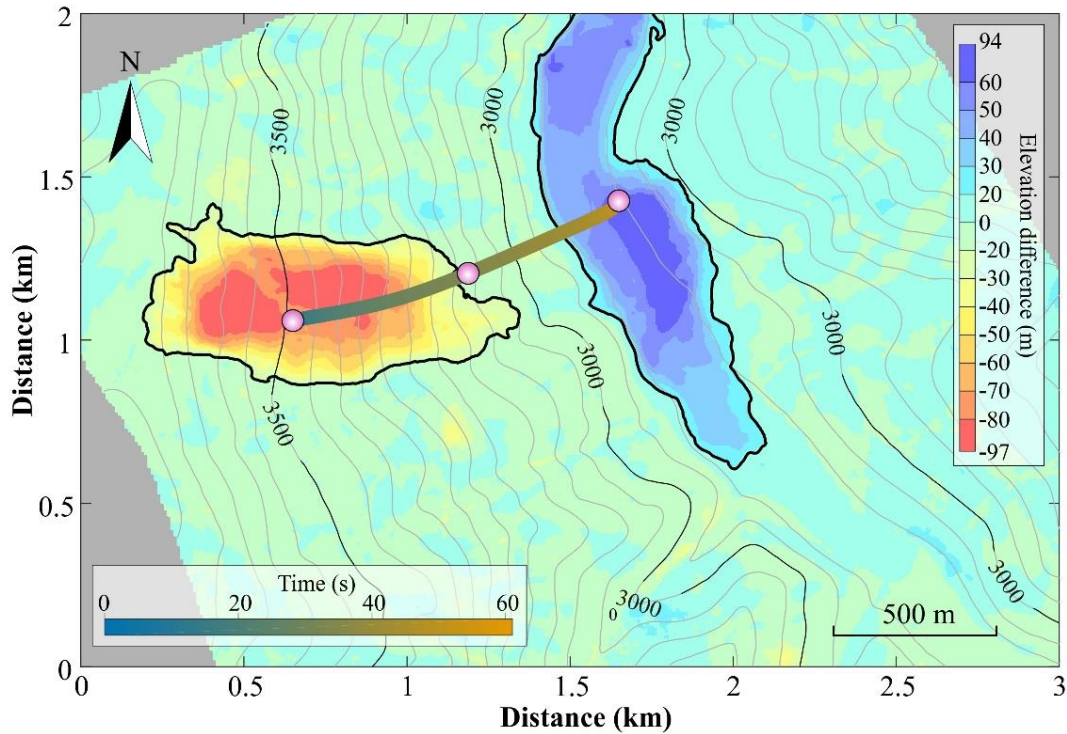
Fig. 10. Reconstructed horizontal trajectory of the Baige landslide from the seismic dynamic inversion. The base map is the elevation difference derived from DEMs and the reconstructed trajectory is shown by the colored dots and connecting timeline.

419   The inversion results show two stages of landslide movement, 34 s of acceleration followed

420   by 27 s of deceleration, which are separated by the vertical dashed black lines in Fig. 8. The sliding

421   mass reached a maximum velocity of 47.4 m/s at the end of the acceleration stage and then rapidly

422   decelerated (Fig. 8c). At c. 50 s, the vertical component shows reverse force and velocity,

423   indicating this was when the main sliding mass traveled over the Jinsha River. The force of the E

424   and V components increases in a nearly linear manner in the first 26 s, but then decreases rapidly.

28

425   The reconstructed horizontal trajectory of the landslide (Fig. 10) indicates that the front of the

426   sliding mass ran up the opposite valley wall after it crossed the Jinsha River.

4.3 Numerical modeling results

428   According to the results of numerical simulation the movement process of the "10.10" Baige

429   landslide can be divided into three stages: (1) sliding (0–20 s); (2) acceleration when entering the

430   river (20–40 s); and (3) diffusion and accumulation (40–80 s). The velocity distribution through

431   each stage of the simulated landslide is shown in Figure 11.

432   At the start of the simulation, the connection between particles inside and outside the sliding

433   source area was broken simultaneously to initiate the landslide, which then rapidly fell with a

434   constant (gravitational) acceleration. Due to the small particle friction coefficient (0.0897),

435   simulated average velocity and average displacement growth rate are both higher than that

436   determined in the inversion until 18 s, but their variation trends are similar. From the square residue

437   results, there is little difference between the simulated and inverted landslide velocity and

438   displacement at this stage, as shown in Fig. 12.

439   In the second stage, the landslide body is moving downwards at a constant acceleration in the

440   simulation, but the inversion shows increased acceleration; so, simulated average velocity and

441   displacement appear to be substantially lower than the inversion. However, the time to reach peak

442   velocity is similar for the simulation (32.8 s) and inversion (32 s). For both velocity and

443   displacement, square residue between the inversion and simulation reaches a maximum in this

444   stage, with S^2 of 2.19×10^2 and 2.88×10^4. At 40 s, the particles at the front edge of the landslide

445 are stationary due to the obstacle provided by the valley wall/mountain slope on the opposite bank

446 of Jinsha River.

447   In the third stage, from 40 s, particles in the middle and rear of the landslide body continue

448 to move downwards, spreading and accumulating along the river, with a constant deceleration.

449 After 60 s, the simulated average displacement reaches 1020 m and levels off thereafter, which

450 corresponds well with the inversion. Most particles in the landslide body have accumulated and

451 are stationary at this stage, but a few particles on the trailing edge are still moving. By 80 s, the

452 average velocity tends to 0, showing that landslide movement has ended. The square residue   of

453 velocity residuals has a secondary peak around 50 s, while the displacement square residue

454 decreases gradually. Overall, the simulated accumulation area is relatively small compared with

455 that derived from DEM differencing, although the location of maximum thickness corresponds

456 well (Fig. 13b). The CSI is calculated as 0.65, which suggests the simulation is moderately good.

457
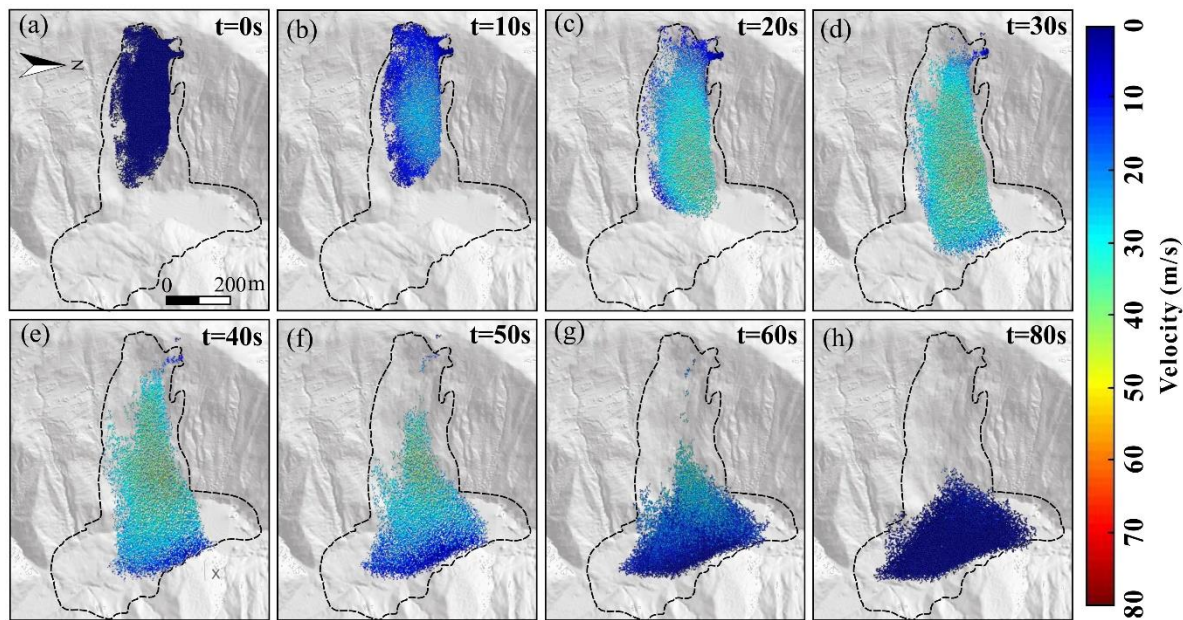
Fig. 11. Simulated landslide velocity distribution calculated in MatDEM. **(a)** t =0 s; **(b)** t =10 s; **(c)** t =20 s; **(d)** t =30 s; **(e)** t =40 s; **(f)** t =50 s; **(g)** t =60 s; **(h)** t =80 s. The digital terrain model (DTM) data of Fig 11. are from the authors' own UAV photography measurements.
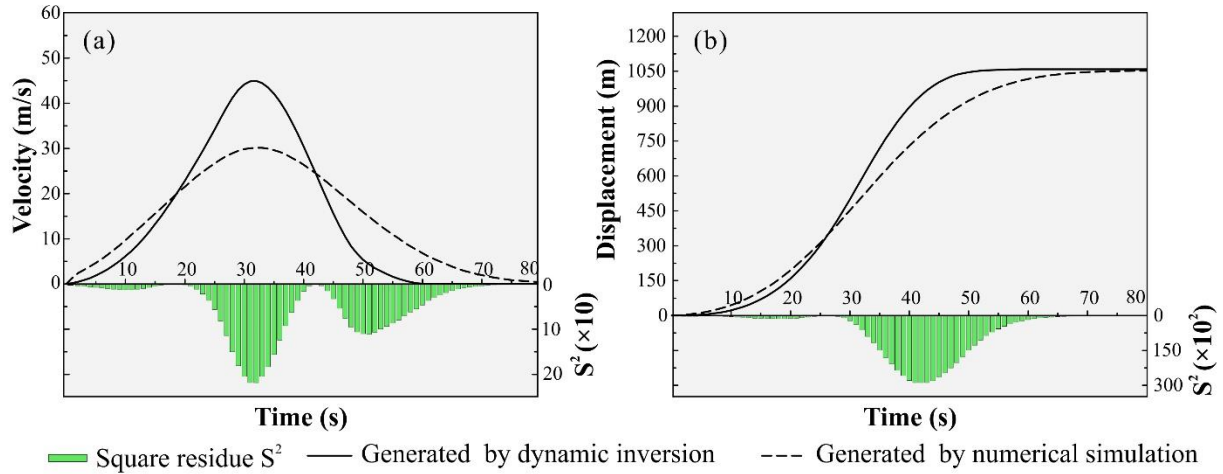
Fig. 12. Comparison of landslide characteristics simulated using discrete element model with inversion results. **(a)** Average velocity; **(b)** Average displacement.
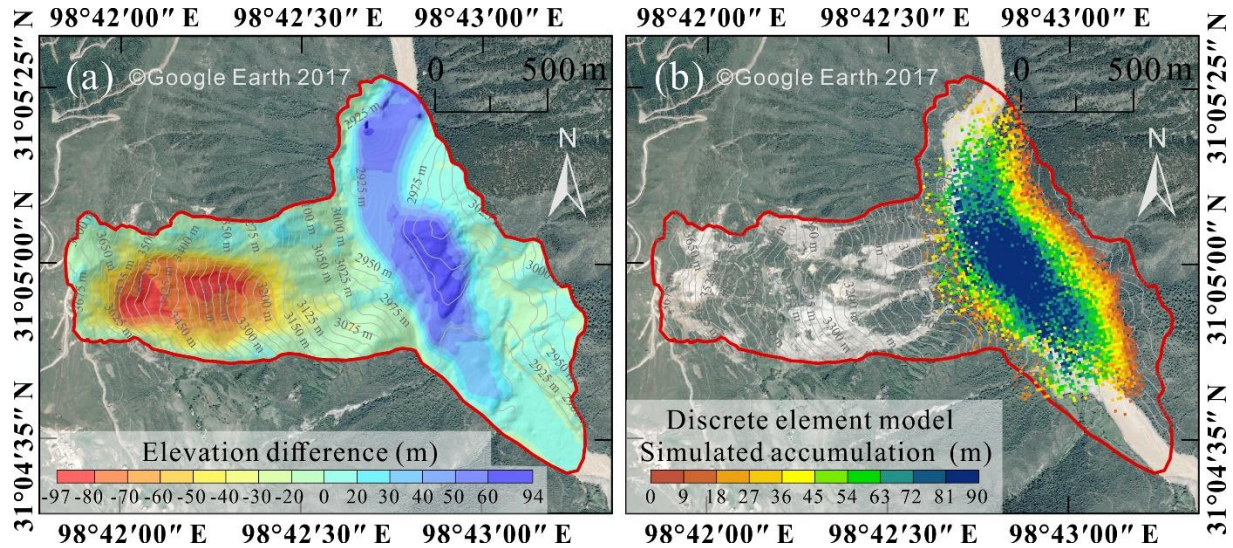
Fig. 13. Comparison of elevation change associated with the Baige landslide. **(a)** Estimated from pre- and post-failure topography; **(b)** Calculated using the discrete element model. The remote sensing image map data of Fig 13.a. and b. are from the © Google Earth 2017.

5. Discussion

5.1 Field observation and dynamic inversion

474   Using the empirical relationships of Chao et al. (2016) and Ekström and Stark (2013), the

475   maximum inverted force of 1.37×10^{11} N gives an estimated sliding mass of 5.5×10^{10} kg and

476   7.4×10^{10} kg, respectively, which are about 1.32 and 1.77 times of our estimation of about 4.2×10^{10}

477   kg from landslide force inversion. We further use a density of 2.4×10^{3} kg/ m^{3} (Zhang et al., 2019)

478   to estimate the volumes corresponding to these masses. The results are 1.75×10^{7}, 2.29×10^{7}, and

479   3.08×10^{7} m^{3}, accounting for 89%, 117%, and 157% of that derived from DEM differences. All

480   estimated volumes are consistent with the DEM-derived volume in general, only that the estimates

481   from empirical relationships are slightly larger. This is not surprising as we used a different

482   frequency band in our inversion (0.006–0.2 Hz) than the two studies (e.g., Ekström and Stark (2013)

483   used the frequency band 0.0067 – 0.0286 Hz(35–150 s)). Previous work has shown that, for a

484   given event, use of different frequency bands produces landslide force histories of different

485   amplitudes (Hibert et al., 2014; Moore et al., 2017; Zhang et al., 2020b). As a comparison, we

486   performed inversion in the frequency band 0.0067 – 0.0286 Hz, which gave a maximum force of

487   1.03×10^{11} N and sliding mass estimates of 4.20×10^{10} kg and 5.60×10^{10} kg that are more consistent

488   with our estimation. The newly estimated volumes from empirical relationships are also closer to

489   the DEM-derived volume, accounting for 89% and 119%, respectively. Since the frequency bands

490   that we used in the two inversions have similar lower cutoff frequencies, both of which include

491   the duration of sliding (Gualtieri and Ekström, 2018; Toney and Allstadt, 2021), the kinematic

492   parameters estimated from both inversion results are essentially similar in their characterization of

493   overall landslide motion. We used the frequency band including relatively higher frequency energy

494   (up to 0.2 Hz) in the inversion to allow finer scale characteristics of the forces and landslide motion

495 to be analyzed (Zhao et al., 2015), such as the near-linear increase of the vertical component force

496 in the first 26 s and subsequent abrupt decrease.

497

498 **5.2 Link with numerical modeling**

499 The numerical simulation combining signal inversion and field data more realistically reflects

500 the landslide process than that based on field data alone. Differencing of pre- and post-landslide

501 terrain data is commonly used to calibrate discrete element simulations; however, it is a recognized

502 limitation that this method does not inform on whether the landslide process is correctly modeled.

503 Different combinations of discrete element parameters may produce very similar superposition

504 results even if the motion processes differ. In this study, the simulation is calibrated by the

505 accumulation characteristics, and then the landslide movement process is further constrained by

506 the inversion of the seismic signal. The final simulation results produced CSI of 0.65, δT_{vmax} of

507 2.5%, δD_{max} of 0.6%, δT of 33.3%, δV_{max} of 33.3% (δT_{vmax}: error of time corresponds to peek

508 velocity from simulated and inversed; δD_{max}: error of peek displacement from simulated and

509 inversed; δT: error of time of landslide from simulated and inversed; δV_{max}: error of peek velocity

510 from simulated and inversed), indicating they reflect the whole process of movement and

511 accumulation well, overcoming the limitations of traditional methods.

512 Differences in the kinetic characteristics of different landslide phases between the numerical

513 simulation and inversion are highlighted using analysis of square residue (Fig. 12). For example,

514 the inversion results simulate the sliding stage (0–20 s) best, the diffusion and deposition stage

515 (40–80 s) second, and the acceleration stage (20–40 s) least. The good simulation of the sliding

516   stage may be due to the fracture zone not yet being completely detached, so landslide movement

517   is dominated by sliding of the whole body, which the theoretical assumption in the inversion

518   approach. In the acceleration stage of large-scale landslides, friction between the sliding rock and

519   soil and the base generates heat, which causes thermal compression and fluidization, leading to

520   soil weakening (Wang et al., 2017, 2018). Reduction in the friction coefficient means the landslide

521   moves faster, however, this factor is not considered in the current inversion model, so it under-

522   estimates peak velocity (Fig. 12). Despite the differences in kinematics, the simulation is

523   essentially consistent with reality in terms of accumulation and movement characteristics.

524   **5.3 Reconstruction of landslide process**

525   The Baige landslide has been the focus of much previous research (Xu et al., 2018; Deng et

526   al., 2019; Fan et al., 2019a; Ouyang et al., 2019; Zhang et al., 2019; Wang et al., 2020c), however,

527   this study is the first analysis that couples seismic signal analysis, dynamic inversion, and

528   numerical simulation. Our approach of multi-method mutual verification effectively reduces the

529   inherent ambiguity of each method, and multi-method analysis improves the rationality and

530   reliability of the results. Based on the characteristics of the "10.10" Baige landslide derived from

531   our seismic signal inversion and discrete element model simulation analysis, we have developed a

532   generic model of landslide dynamics (Figure 14). Our findings show the landslide was triggered

533   by detachment of the weathered layer with severe top fault segmentation and the landslide process

534   comprised four stages: initiation, main slip, blocking, and deposition, as outlined below.

535   1. Initiation stage (Fig. 14a): The fracture zone on the upper part of the first-level platform

536   loses stability and slides down under the action of gravity. Landslide debris is hindered by friction

537 on the surface of the main sliding zone, so the landslide body moves relatively slowly. Increasing

538 debris accumulates on the first-level platform and the lower main sliding area, which increases

539 instability of the weathered layer, and other debris continues to fall downslope. The surface

540 weathering layer of the main sliding area starts to slide, and the landslide body forms after the first

541 fracture in the fracture development zone. Cascading from the initial fracture, continuous

542 fracturing and sliding of the shear zone causes the landslide body to gradually increase; sliding of

543 the top surface of the main sliding zone increases the scale of the landslide body. Downward sliding

544 gradually accelerates as the landslide body increases, but friction in the main sliding area then acts

545 to decelerate the mass; the deceleration process can be seen in the signal recorded at seismic station

546 GZI (Fig. 7). As a result, acceleration increases slowly over c. 10 s; this is evident in both the

547 inversion and numerical simulation results.

548   2. Main slip stage (Fig. 14b): The main sliding area gradually loses stability and slides rapidly

549 under the control of structural surfaces formed by weathering; the landslide body passes through

550 the main sliding area and enters the wide and gentle second level platform where resistance is

551 relatively high. After crossing the second level platform, the landslide enters the slip resistance

552 zone where the degree of weathering is relatively weak, so the scouring action of the landslide

553 body drives resistance. The effect of both sliding and anti-slip zones on the landslide body is

554 relatively weak and is characterized well by the seismic signal in the time domain and the inverted

555 acceleration curve. The initial sliding stage of the main sliding zone is reflected in the gradually

556 increasing acceleration that peaks when the landslide body reaches the second level platform, and

557 then decreases. When acceleration is approximately zero, the front part of the landslide has entered

558   the river, and velocity of the landslide body peaks; the timing of maximum velocity in the inversion

559   and simulation is consistent, at 32 s and 34 s, respectively (Fig. 12a).

560   3. Blocking stage (Crawling up the opposite valley wall) (Fig. 14c): After passing through the

561   anti-slip area, the landslide detaches at high speed at an altitude of c. 2950 m and loses support of

562   the ground surface. Part of the landslide body accumulates in the river and part hits the opposite

563   (left) bank of the Jinsha River at a high speed and crawls upwards against the valley slope. During

564   the upward movement, landslide debris spreads upstream and downstream, scouring the left bank

565   of the river (SA3 in Fig. 1c) and a small area of the right bank (SA4 in Fig. 1c). Landslide debris

566   reaches a maximum elevation of 3045 m on the opposite slope, then slides downslope under the

567   action of gravity, forming debris strips like the scratches found on the sliding surface. Some debris

568   remains on the relatively gentle slope of the left bank. The main feature of this process is that the

569   action of gravity changes the force of the landslide body from dynamic to resistance; this is well

570   reflected in the time-domain seismic curve and inversion results (Fig. 8), where the acceleration

571   switches rapidly from increasing to decreasing over c. 10 s. As the upward crawling situation was

572   not considered in the model design, the numerical simulation failed to describe the process.

573   4. Deposition stage (Falling back and accumulation) (Fig. 14d): Debris rapidly falls back

574   down under the action of gravity, colliding with debris in the traction area of the river channel and

575   interacting with stream flow to form a jet stream. Some finer particles in the landslide body mix

576   with the sandblasting water to form a water-sand jet that discharges diagonally across the river,

577   toward the downstream left bank (SA5 in Fig. 1c) and upstream right bank (SA4 in Fig. 1c). Most

578   of the detrital material stops moving and is deposited in the river channel, forming a barrier dam

579   that starts to pond water. Under gravity and the action of water flow, small fragments at the top of

580   the dam body lose stability and form a secondary slip zone (SA1 and SA2 in Fig. 1c) that becomes

581   a drainage channel. The acceleration change during this downturn is roughly the same as the

582   change trend of the main sliding phase. Acceleration first gradually increases and then decreases

583   to zero before entering the deceleration phase. The seismic curve in the time domain and the

584   inverted acceleration curve both characterize this process well, and the inversion results give a

585   duration of c. 10 s.

586
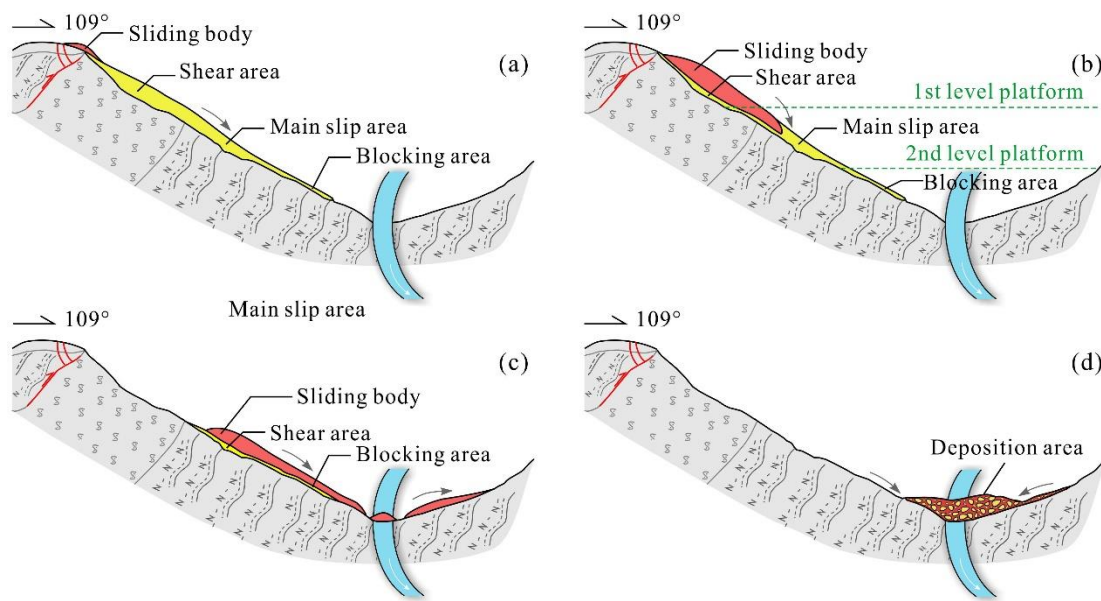
587 **Fig. 14.** Schematic diagram of the Baige landslide model. **(a)** Stage 1 –initiation; **(b)** Stage 2 –
588 main slip; **(c)** Stage 3 – crawling up against the slope (blocking); **(d)** Stage 4 – falling back and
589 accumulation (deposition).

590

591 ## 5.4 Research contribution

592   Post-event geological survey can examine depositional characteristics of the landslide and

593   weathering and fracture conditions of rocks in the slide source area, which provides some

594   information for understanding landslide causal processes. The seismic signal provides some

information on landslide evolution, with the low-frequency component reflecting the overall movement trend of the landslide and the high-frequency component reflecting detailed characteristics of the movement process. Experienced researchers can reconstruct the landslide process using a combination of geological survey and seismic signal analysis. However, the propagation effect of the stratum means that the seismic signal does not completely correspond to landslide movement and may generate false images, as well as confounding precise determination of landslide start time and duration.

Landslide dynamic inversion based on the long-wavelength information of the seismic signal eliminates the propagation effect which allows the dynamic parameter curve of the landslide to be obtained, giving a relatively accurate determination of landslide start and end time and event duration. The dynamic inversion result reflects the change process of the overall movement trend of the landslide (the low-frequency trend) and can be used to verify the results of combined geological survey and seismic signal analysis. The low-frequency (0~0.2 Hz) component of dynamic parameters, as provided by dynamic inversion, can guide the all band frequency motion, constraining the high frequency (>0.2 Hz) movement, analysis of the landslide process, which helps to reduce ambiguity.

The accuracy of numerical simulation results depends on scientific models and accurate parameters. When static parameters such as pre- and post-landslide topography are used to select parameters and constrain results of numerical simulation, there are often multiple solutions. The accuracy of the landslide dynamic with time evolution process will not be determined using only the calibration of the depositional morphology, because different velocities, evolutionary processes may produce similar accretionary landforms (An et al. 2021; Mergili et al. 2017), especially for large scale landslides like Baige, which occur next to deep-incised valleys. Compared with the study of An et al. (2021), which mainly focuses on force time history inversion, we further added the velocity and displacement characteristics retrieved from seismic signals to conduct dynamic quantitative constraints on dynamic parameters and improve the credibility of numerical simulation, so as to carry out efficient simulation of landslide process. The improved simulation

622   allows in-depth analysis of frequency motion characteristics of the landslide, such as speed change,

623   characteristics of each stage, etc. These characteristics can also be used to verify and optimize the

624   landslide process to improve analysis results.

625   Each of the three methods has disadvantages which may lead to errors and ambiguities in

626   analyzing landslides. However, the combined use and mutual verification of the different methods

627   can effectively avoid ambiguity and improve the reasonableness of results.

628

6. Conclusions

630   In this study, we used on-site geological survey, landslide seismic signal analysis, dynamic

631   inversion, and numerical simulation to provide a comprehensive analysis of "10.10" Baige

632   landslide. We used short-time Fourier transform (STFT) and PSD to analyze the seismic signals

633   for Baige landslide. We then reconstructed the landslide force history by direct deconvolution of

634   the observed seismograms with Green's functions. We then developed a method that use seismic

635   inversion to constrain and calibrate the numerical input parameters using DEM. After calibrating

636   the parameters of the numerical models, the dynamic process of the "10.10" Baige landslide was

637   analysed. Nevertheless, several key issues, such as friction coefficient decreases as the landslide

638   progresses, base entrainment, particle breakage, are not considered in the DEM, which leads the

639   difference between simulation and inversion, should be considered in future research.

640

7. Appendix 1

Macro and Micro Conversion Formula of Discrete Element Model

643   There is an analytical solution between the macro and micromechanical parameters of the

644   tightly packed discrete element model, that is, the conversion formula proposed by Liu et al. (2013).

645   For the linear elastic model, there are five micromechanical parameters, that is, the normal stiffness

646   (K_n), shear stiffness (K_s), breaking displacement (X_b), shear resistance (F_{s0}), coefficient of friction

647   (μ_p) can be defined by Young's modulus (E), Poisson's ratio (v), tensile strength (T_u), compressive

strength (C_u) and coefficient of intrinsic friction (μ_i). The conversion formulas are as follows:

$$K_n = \frac{E}{\sqrt{3(1-2v)(1+v)}} \tag{A1}$$

$$K_s = \frac{E(1-4v)}{\sqrt{3(1-2v)(1+v)}} \tag{A2}$$

$$X_b = \frac{2K_n + K_s}{2\sqrt{3}K_n(K_n + K_s)}T_u d \tag{A3}$$

$$F_{s0} = (\frac{1}{4} - \frac{\sqrt{3}}{4}\mu_p)C_u d \tag{A4}$$

$$\mu_p = \frac{-3\sqrt{3} + \sqrt{3}I}{3+3I}, I = [(1+\mu_i)^{0.5} + \mu_i]^2 \tag{A5}$$

8. Acknowledgements

Data availability

All raw data can be provided by the corresponding authors upon request.

Author contributions

The authors of this manuscript entitled "Combining seismic signal dynamic inversion and numerical modeling improves landslide process reconstruction" are Yan Yan, Yifei Cui, Jiaojiao

Zhou, Xinghui Huang, Wengang Zhang, Shuyao Yin, Jian Guo, Sheng Hu. Yan Yan is the first author, is responsible for most of the work and paper writing in this research. Yifei Cui is the second author and the corresponding author, is responsible for the processing and verification of the article data. JiaoJiao Zhou and Xinghui Huang is the third, fourthauthor and is responsible for the production of the article figures and tables. Wengang Zhang is responsible for checking the overall logical structure of the article. Shuyao Yin and Jian Guo is responsible for the numerical simulations. Sheng Hu is responsible for reviewing and editing the manuscript.

Competing interests

The authors declare that they have no conflict of interest.

9. References

Allstadt, K.: Extracting source characteristics and dynamics of the August 2010 Mount M eager landslide from broadband seismograms, J. Geophys. Res.-Earth, 118, 1472–149 0, https://doi.org/10.1002/jgrf.20110, 2013.

An, H. C., Ouyang, C. J., Zhao, C., and Zhao, W.: Landslide dynamic process and para meter sensitivity analysis by discrete element method: the case of Turnoff Creek roc k avalanche, J. Mt. Sci., 17, 1581-1595, https://doi.org/10.1007/s11629020-5993-7, 20 20.

An, H. C, Ouyang, C. J, Zhou, S.: Dynamic process analysis of the Baige landslide by t he combination of DEM and long-period seismic waves, Landslides, 18, 1625-1639, https://doi.org/10.1007/s10346-020-01595-0, 2021.

Brodsky, E. E., Gordeev, E., and Kanamori, H.: Landslide basal friction as measured by seismic waves, Geophys. Res. Lett., 30, 2236, https://doi.org/10.1029/2003GL018485, 2003.

Chao, W. A., Zhao, L., Chen, S. C., Wu, Y. M., Chen, C. H., and Huang, H. H.: Seis mology-based early identification of dam-formation landquake events, Sci. Rep., 6, 1 9259, https://doi.org/10.1038/srep19259, 2016.

Chao, W. A., Wu, Y. M., Zhao, L., Chen, H., Chen, Y. G., Chang, J. M., and Lin, C. M.: A first near real-time seismology-based landquake monitoring system, Sci. Rep., 7, 43510, https://doi.org/10.1038/srep43510, 2017.

Chen, C. H., Chao, W. A., Wu, Y. M., Zhao, L., Chen, Y. G., Ho, W. Y., Lin, T. L., Kuo, K. H., and Chang, J. M.: A seismological study of landquakes using a real-ti

me broad-band seismic network, Geophys. J. Int., 194, 885-898, http://doi.org/10.1093 /gji/ggt121, 2013.

Dahlen, F. A.: Single-force representation of shallow landslide sources, B. Seismol. Soc. Am., 83, 130–143, http://doi.org/10.1785/BSSA0830010130, 1993.

Dammeier, F., Moore, J. R., Hammer, C., Haslinger, F., and Loew, S.: Automatic detecti on of alpine rockslides in continuous seismic data using hidden Markov models, J. Geophys. Res.-Earth, 121, 351-371, http://doi.org/10.1002/2015jf003647, 2016.

Darlington, W.J., Ranjith, P.G., and Choi, S.K.: The Effect of Specimen Size on Strength and Other Properties in Laboratory Testing of Rock and Rock-Like Cementitious Br ittle Materials, Rock Mech Rock Eng, 44, 513, https://doi.org/10.1007/s00603-011-016 1-6, 2011.

Deng, J. J., Gao, Y. J., Yu, Z. Q., and Xie, H. P.: Analysis on the Formation Mechanis m and Process of Baige Landslides Damming the Upper Reach of Jinsha River,Chin a, Adv. Eng. Sci., 51, 9-16, http://doi.org/10.15961/j.jsuese.201801438, 2019.(In Chine se)

Ekström, G., and Stark, C. P.: Simple scaling of catastrophic landslide dynamics, Science. 339, 1416–1419. https://doi.org/10.1126/science.1232887, 2013.

Fan, X., Yang, F., Subramanian, S. S., Xu, Q., Feng, Z., Mavrouli, O., Peng, M., Ouyan g, C., Jansen, D., and Huang, R.: Prediction of a multi-hazard chain by an integrate d numerical simulation approach: the Baige landslide, Jinsha River, China, Landslide s, 17, 147-164, http://doi.org/10.1007/s10346-019-01313-5, 2019a.

Fan, X., Xu, Q., Liu, J., Subramanian, S. S., He, C., Zhu, X., and Zhou, L.: Successful early warning and emergency response of a disastrous rockslide in Guizhou province, China, Landslides, 16, 2445–2457, https://doi.org/10.1007/s10346-019-01269-6, 2019b.

Favreau, P., Mangeney, A., Lucas, A., Crosta, G., and Bouchut, F.: Numerical modeling of landquakes, Geophys. Res. Lett., 37, L15305, http://doi.org/10.1029/2010gl043512, 2010.

Feng, Z.: The seismic signatures of the 2009 Shiaolin landslide in Taiwan, Nat. Hazards Earth Syst. Sci., 11, 1559-1569, http://doi.org/10.5194/nhess-11-1559-2011, 2011.

Feng, Z. Y., Lo, C. M., and Lin, Q. F.: The characteristics of the seismic signals induce d by landslides using a coupling of discrete element and finite difference methods, Landslides, 14, 661-674, http://doi.org/10.1007/s10346-016-0714-6, 2016.

Froude, M. J., and Petley, D. N.: Global fatal landslide occurrence from 2004 to 2016, Nat. Hazards Earth Syst. Sci., 18, 2161-2181, http://doi.org/10.5194/nhess-18-2161-201 8, 2018.

Fuchs, F., Lenhardt, W., and Bokelmann, G.: Seismic detection of rockslides at regional scale: examples from the Eastern Alps and feasibility of kurtosis-based event locatio n, Earth Surf. Dynam., 6, 955-970, http://doi.org/10.5194/esurf-6-955-2018, 2018.

Fukao, Y.: Single-force representation of earthquakes due to landslides or the collapse of caverns, Geophys. J. Int., 122, 243–248, https://doi.org/10.1111/j.1365-246X.1995.tb03 551.x, 1995.

740 Gualtieri, L., and Ekström, G.: Broad-band seismic analysis and modeling of the 2015 T
741   aan Fjord, Alaska landslide using Instaseis, Geophys. J. Int., 213, 1912–1923, https://
742   doi.org/10.1093/gji/ggy086, 2018.

743 Hasegawa, H. S., and Kanamori, H.: Source mechanism of the magnitude 7.2 Grand Ban
744   ks earthquake of November 1929: Double couple or submarine landslide?, B. Seismo
745   l. Soc. Am., 77, 1984–2004, 1987.

746 Helmstetter, A., and Garambois, S.: Seismic monitoring of Séchilienne rockslide (French
747   Alps): Analysis of seismic signals and their correlation with rainfall, J. Geophys. Re
748   s., 115, F03016, http://doi.org/10.1029/2009jf001532, 2010.

749 Hencher, S. R., Richards, L. R.: Assessing the Shear Strength of Rock Discontinuities at
750   Laboratory and Field Scales, Rock Mech Rock Eng, 48, 883-905, https://doi.org/10.1
751   007/s00603-014-0633-6, 2014.

752 Hibert, C., Ekström, G., and Stark, C. P.: Dynamics of the Bingham Canyon Mine lands
753   lides from seismic signal analysis, Geophys. Res. Lett., 41, 4535–4541, https://doi.org
754   /10.1002/2014GL060592, 2014.

755 Hibert, C., Stark, C. P., and Ekström, G.: Dynamics of the Oso-Steelhead landslide from
756   broadband seismic analysis, Nat. Hazards Earth Syst. Sci., 15, 1265–1273, https://doi.
757   org/10.5194/nhess-15-1265-2015, 2015.

758 Hoek E.: Rock engineering course notes by Evert Hoek. http://www.rocscience.com/educat
759   ion/hoeks_corner, 2000.

760 Jiang, Y., Wang, G., and Kamai, T.: Fast shear behavior of granular materials in ring-sh
761   ear tests and implications for rapid landslides, Acta Geotech., 12, 645-655, http://doi.
762   org/10.1007/s11440-016-0508-y, 2016.

763 Kääb, A., Leinss, S., Gilbert, A., Bühler, Y., Gascoin, S., Evans, S. G., Bartelt, P., Bert
764   hier, E., Brun, F., Chao, W. A., Farinotti, D., Gimbert, F., Guo, W., Huggel, C., Ka
765   rgel, J.S., Leonard, G.J., Tian, L., Treichler, D., and Yao, T.: Massive collapse of t
766   wo glaciers in western Tibet in 2016 after surge-like instability, Nat. Geosci., 11, 11
767   4–120, https://doi.org/10.1038/s41561-017-0039-7, 2018.

768 Kanamori, H., and Given, J.W.: Analysis of long-period seismic waves excited by the M
769   ay 18, 1980, eruption of Mount St. Helens—A terrestrial monopole?, J. Geophys. Re
770   s.-Sol. Ea., 87, 5422–5432, https://doi.org/10.1029/JB087iB07p05422, 1982.

771 Kanamori, H., Given, J. W., and Lay, T.: Analysis of seismic body waves excited by th
772   e Mount St. Helens eruption of May 18, 1980, J. Geophys. Res.-Sol. Ea., 89, 1856–
773   1866, https://doi.org/10.1029/JB089iB03p01856, 1984.

774 Kao, H., Kan, C. W., Chen, R. Y., Chang, C. H., Rosenberger, A., Shin, T .C., Leu, P.
775   L., Kuo, K. W., and Liang, W. T.: Locating, monitoring, and characterizing typhoon
776   -induced landslides with real-time seismic signals, Landslides, 9, 557-563, http://doi.o
777   rg/10.1007/s10346-012-0322-z, 2012.

778 Li, C. Y., Wang, X. C., He, C. Z., Wu, X., Kong, Z. Y., and Li, X. L. China National
779   Digital Geological Map (Public Version at 1:200 000 Scale) Spatial Database(V1). D
780   evelopment and Research Center of China Geological Survey; China Geological Surv

781 ey[producer], 1957. National Geological Archives of China [distributor], 2019-06-30.
782   https://doi.org/10.23650/data.A.2019.NGA120157.K1.1.1.V1, 2019a.

783 Li, W., Chen, Y., Liu, F., Yang, H., Liu, J., and Fu, B.: Chain-style landslide hazardous
784   process: Constraints from seismic signals analysis of the 2017 Xinmo landslide, SW
785   China, J. Geophys. Res.-Sol. Ea., 124, 2025–2037, https://doi.org/10.1029/2018JB0164
786   33, 2019b.

787 Li, Z., Huang, X., Xu, Q., Yu, D., Fan, J., and Qiao, X.: Dynamics of the Wulong land
788   slide revealed by broadband seismic records, Earth, Planets Space, 69, 27, https://doi.
789   org/10.1186/s40623-017-0610-x, 2017.

790 Li, Z., Huang, X., Yu, D., Su, J., and Xu, Q.: Broadband-seismic analysis of a massive
791   landslide in southwestern China: Dynamics and fragmentation implications, Geomorph
792   ology, 336, 31–39. https://doi.org/10.1016/j.geomorph.2019.03.024, 2019c.

793 Liu, C., Pollard, D. D., and Shi, B.: Analytical solutions and numerical tests of elastic a
794   nd failure behaviors of close-packed lattice for brittle rocks and crystals, J. Geophys.
795   Res.-Sol. Ea., 118, 71-82, https://doi.org/10.1029/2012JB009615, 2013.

796 Liu, C., Xu, Q., Shi, B., Deng, S., and Zhu, H.: Mechanical properties and energy conve
797   rsion of 3D close-packed lattice model for brittle rocks, Comput. Geosci., 103, 12-20,
798   https://doi.org/10.1016/j.cageo.2017.03.00, 2017.

799 Liu, C., Fan, X., Zhu, C., and Shi, B.: Discrete element modeling and simulation of 3-D
800   imensional large-scale landslide-Taking Xinmocun landslide as an example, J. Eng. G
801   eol, 27, 1362-1370, https://doi.org/10.13544/j.cnki.jeg.2018-234, 2019. (In Chinese)

802 Lo, C. M., Lin, M. L., Tang, C. L., and Hu, J. C.: A kinematic model of the Hsiaolin
803   landslide calibrated to the morphology of the landslide deposit, Eng. Geol., 123, 22-
804   39, https://doi.org/10.1016/j.enggeo.2011.07.002, 2011.

805 McNamara, D.E., Buland, R.P., 2004. Ambient Noise Levels in the Continental United St
806   ates. Bull. Seismol. Soc. Am. 94, 1517–1527. https://doi.org/10.1785/012003001

807 Mergili, M., Fischer, J. T., Krenn, J., and Pudasaini, S. P.: r. avaflow v1, an advanced o
808   pen-source computational framework for the propagation and interaction of two-phase
809   mass flows, Geosci. Model Dev, 10, 553-569, https://doi.org/10.5194/gmd-10-553-201
810   7, 2017.

811 Mergili, M., Emmer, A., Juřicová A., Cochachin, A., Fischer, J. T., Huggel, C., and Pud
812   asaini, S. P.: How well can we simulate complex hydro-geomorphic process chains?
813   The 2012 multi-lake outburst flood in the Santa Cruz Valley (Cordillera Blanca, Per
814   ú), Earth Surf Process Landf, 43, 1373-1389, https://doi.org/10.1002/esp.4318, 2017.

815 Moore, J. R., Pankow, K. L., Ford, S. R., Koper, K. D., Hale, J. M., Aaron, J., and Lar
816   sen, C.F.: Dynamics of the Bingham Canyon rock avalanches (Utah, USA) resolved
817   from topographic, seismic, and infrasound data, J. Geophys. Res.-Earth, 122, 615–64
818   0, https://doi.org/10.1002/2016JF004036, 2017.

819 Moretti, L., Mangeney, A., Capdeville, Y., Stutzmann, E., Huggel, C., Schneider, D., and
820   Bouchut, F.: Numerical modeling of the Mount Steller landslide flow history and of

the generated long period seismic waves, Geophys. Res. Lett., 39, L16402, https://do i.org/10.1029/2012GL052511, 2012.

Moretti, L., Allstadt, K., Mangeney, A., Capdeville, Y., Stutzmann, E., and Bouchut, F.: Numerical modeling of the Mount Meager landslide constrained by its force history derived from seismic data, J. Geophys. Res.-Sol. Ea., 120, 2579–2599, https://doi.org/ 10.1002/2014JB011426, 2015.

Muceku, Y., Korini, O., and Kuriqi, A.: Geotechnical analysis of hill's slopes areas in h eritage town of Berati, Albania. Period. Polytech., Civ. Eng. 60, 61-73, https://doi.org/ 10.3311/PPci.7752, 2016.

Ouyang, C. J., An, H. C., Zhou, S., Wang, Z. W., Su, P. C., and Wang, D. P.: Insights from the failure and dynamic characteristics of two sequential landslides at Baige v illage along the Jinsha River, China, Landslides, 16, 1397-1414, https://doi.org/10.1007 /s10346-019-01177-9, 2019.

Pastor, M., Blanc, T., Haddad, B., Petrone, S., Sanchez, M. M., Drempetic, V., Issler, D., Crosta, G. B., Cascini, L., Sorbino, G., and Cuomo, S.: Application of a SPH dept hintegrated model to landslide run-out analysis, Landslides, 11, 793812, https://doi.or g/10.1007/s10346-014-0484-y, 2014.

Peterson, J.R., 1993. Observations and modeling of seismic background noise, U.S. Geolo gical Survey Open-File Report 93-322. https://doi.org/10.3133/ofr93322.

Pitman, E. B., Nichita, C. C., Patra, A., Bauer, A., Sheridan, M., and Bursik, M.: Comp uting granular avalanches and landslides, Phys. Fluids., 15, 3638-3646, ,https://doi.org/ 10.1063/1.1614253, 2003.

Sakals, M. E., Geertsema, M., Schwab, J. W., and Foord, V. N.: The Todagin Creek lan dslide of October 3, 2006, Northwest British Columbia, Canada, Landslides, 9, 107-1 15, http://doi.org/10.1007/s10346-011-0273-9, 2011.

Schöpa, A., Chao, W. A., Lipovsky, B. P., Hovius, N., White, R. S., Green, R. G., and Turowski, J. M.: Dynamics of the Askja caldera July 2014 landslide, Iceland, from seismic signal analysis: precursor, motion and aftermath, Earth Surf. Dynam., 6, 467 –485, https://doi.org/10.5194/esurf-6-467-2018, 2018.

Shen, W., Li, T., Li, P., and Lei, Y.: Numerical assessment for the efficiencies of check dams in debris flow gullies: A case study, Comput. Geotech., 122, 103541, https://doi. org/10.1016/j.compgeo.2020.103541, 2020.

Sheng, M., Chu, R., Wang, Y., and Wang, Q.: Inversion of source mechanisms for singl e-force events using broadband waveforms, Seismol. Res. Lett., 91, 1820–1830, https: //doi.org/10.1785/0220190349, 2020.

Soga, K., Alonso, E., Yerro, A., Kumar, K., and Bandara, S.: Trends in large-deformatio n analysis of landslide mass movements with particular emphasis on the material poi nt method, Géotechnique, 66, 1-26, https://doi.org/10.1680/jgeot.15.lm.005, 2016.

Toney, L., Allstadt, K.E.: lsforce: A Python‑Based Single‑Force Seismic Inversion Frame

work for Massive Landslides. Seismol. Res. Lett. 92, 2610–2626. https://doi.org/10.17

85/0220210004, 2021.

Walter, M., Arnhardt, C., and Joswig, M.: Seismic monitoring of rockfalls, slide quakes, and fissure development at the Super-Sauze mudslide, French Alps, Eng. Geol., 128, 12-22, http://doi.org/10.1016/j.enggeo.2011.11.002, 2012.

Wang, L. Q., Yin, Y. P., Huang, B. L., and Dai, Z. W.: Damage evolution and stability analysis of the Jianchuandong Dangerous Rock Mass in the Three Gorges Reservoir Area, Eng. Geol., 265, 105439, http://dx.doi.org/10.1016/j.enggeo.2019.105439, 2020a.

Wang, L., Wu, C. Z., Gu, X., Liu, H. L., Mei, G. X., and Zhang, W. G.: Probabilistic stability analysis of earth dam slope under transient seepage using multivariate adapti ve regression splines, Bull. Eng. Geol. Environ., 79, 2763–2775, http://dx.doi.org/10.1 007/s10064-020-01730-0, 2020b.

Wang, R.: A simple orthonormalization method for stable and efficient computation of G reen's functions, B. Seismol. Soc. Am., 89, 733–741, 1999.

Wang, W., Yin, Y., Zhu, S., Wang, L., Zhang, N., and Zhao, R.: Investigation and num erical modeling of the overloading-induced catastrophic rockslide avalanche in Baige, Tibet, China, Bull. Eng. Geol. Environ., 79, 1765-1779, https://doi.org/10.1007/s10064 -019-01664-2, 2020c.

Wang, Y. F., Dong, J. J., Cheng, Q. G.: Velocity-dependent frictional weakening of large rock avalanche basal facies: Implications for rock avalanche hypermobility?, J. Geop hys. Res.-Sol. Ea., 122, 1648-1676, https://doi.org/10.1002/2016JB013624, 2017.

Wang, Y. F., Dong, J. J., Cheng, Q. G.: Normal stress-dependent frictional weakening of large rock avalanche basal facies: Implications for the rock avalanche volume effec t, J. Geophys. Res.-Sol. Ea., 123, 3270-3282, https://doi.org/10.1002/ 2018JB015602, 2 018.

Xu, Q., Zheng, G., Li, W. L., He, C. Y., Dong, X. J., Guo, C., and Feng, W. K.: Stud y on Successive Landslide Damming Events of Jinsha River in Baige Village on Oc tober 11 and November 3, 2018, J. Eng. Geo, 26, 1534-1551, https://doi.org/10.1354 4/j.cnki.jeg.2018-406, 2018. (In Chinese)

Yamada, M., Matsushi, Y., Chigira, M., Mori, J.: Seismic recordings of landslides caused by Typhoon Talas (2011), Japan, Geophys. Res. Lett., 39, L13301, http://doi.org/10. 1029/2012gl052174, 2012.

Yamada, M., Kumagai, H., Matsushi, Y., and Matsuzawa, T.: Dynamic landslide processe s revealed by broadband seismic records, Geophys. Res. Lett., 40, 2998–3002, https:/ /doi.org/10.1002/grl.50437, 2013.

Yamada, M., Mangeney, A., Matsushi, Y., and Moretti, L.: Estimation of dynamic frictio n of the Akatani landslide from seismic waveform inversion and numerical simulatio n, Geophys. J. Int., 206, 1479–1486. https://doi.org/10.1093/gji/ggw216, 2016.

Yamada, M., Mangeney, A., Matsushi, Y., and Matsuzawa, T.: Estimation of dynamic friction and movement history of large landslides, Landslides, 15, 1963–1974, https://doi.org/10.1007/s10346-018-1002-4, 2018.

Yan, Y., Cui, Y., Guo, J., Hu, S., Wang, Z., and Yin, S.: Landslide reconstruction using seismic signal characteristics and numerical simulations: Case study of the 2017 "6.24" Xinmo landslide, Eng. Geol., 270, 105582, http://doi.org/10.1016/j.enggeo.2020.105582, 2020a.

Yan, Y., Cui, Y., Tian, X., Hu, S., Guo, J., Wang, Z., Yin, S., and Liao, L.: Seismic signal recognition and interpretation of the 2019 "7.23" Shuicheng landslide by seismogram stations, Landslides, 17, 1191-1206, http://doi.org/10.1007/s10346-020-01358-x, 2020b.

Yan, Yan., Yifei, Cui., Dingzhu, Liu., Hui, Tang., Yongjian, Li., Xin, Tian., Lei, Zhang., and Sheng, Hu.: Seismic Signal Characteristics and Interpretation of the 2020 "6.17" Danba Landslide Dam Failure Hazard Chain Process , Landslides, 18(6): 2175-2192. https://doi.org/10.1007/s10346-021-01657-x, 2021.

Yu, D., Huang, X., and Li, Z.: Variation patterns of landslide basal friction revealed from long-period seismic waveform inversion, Nat. Hazards, 100, 313–327, https://doi.org/10.1007/s11069-019-03813-y, 2020.

Zhang, L., Xiao, T., He, J., and Chen, C.: Erosion-based analysis of breaching of Baige landslide dams on the Jinsha River, China, in 2018, Landslides, 16, 1965-1979, https://doi.org/10.1007/s10346-019-01247-y, 2019.

Zhang, S. L., Yin, Y. P., Hu, X. W., Wang, W. P., Zhang, N., Zhu, S. N., and Wang, L. Q.: Dynamics and emplacement mechanisms of the successive Baige landslides on the Upper Reaches of the Jinsha River, China, Eng. Geol., 278, 105819, http://dx.doi.org/10.1016/j.enggeo.2020.105819, 2020a.

Zhang, Z., He, S., Liu, W., Liang, H., Yan, S., Deng, Y., Bai, X., and Chen, Z.: Source characteristics and dynamics of the October 2018 Baige landslide revealed by broadband seismograms, Landslides, 16, 777-785, http://doi.org/10.1007/s10346-019-01145-3, 2019.

Zhang, Z., He, S., and Li, Q.: Analyzing high-frequency seismic signals generated during a landslide using source discrepancies between two landslides, Eng. Geol., 272, 105640, https://doi.org/10.1016/j.enggeo.2020.105640, 2020b.

Zhao, J., Moretti, L., Mangeney, A., Stutzmann, E., Kanamori, H., Capdeville, Y., Calder, E. S., Hibert, C., Smith, P. J., Cole, P., and Lefriant, A.: Model space exploration for determining landslide source history from long-period seismic data, Pure Appl. Geophys., 172, 389–413, https://doi.org/10.1007/s00024-014-0852-5, 2015.

Zhao, J., Ouyang, C. J., Ni, S. D., Chu, R. S., and Mangeney, A.: Analysis of the 2017 June Maoxian landslide processes with force histories from seismological inversion and terrain features, Geophys. J. Int., 222, 1965–1976, https://doi.org/10.1093/gji/ggaa226, 2020.

938 Zhou, L., Fan, X., Xu, Q., Yang, F., and Gou, C.: Numerical simulation and hazard pre
939   diction on movement process characteristics of Baige landslide in Jinsha river, Eng.
940   Geol., 27, 1395-1404, https://doi.org/10.13544/j.cnki. jeg. 2019-037, 2019. (In Chines
941   e)